Atomization and Sprays, 23 (11): 1001–1048 (2013)

DIRECT NUMERICAL AND LARGE-EDDY SIMULATION OF PRIMARY ATOMIZATION IN COMPLEX GEOMETRIES

Olivier Desjardins,* Jeremy O. McCaslin, Mark Owkes, & Peter Brady

Sibley School of Mechanical and Aerospace Engineering, Cornell University, Ithaca, New York 14853-7501, USA

*Address all correspondence to Olivier Desjardins
E-mail: olivier.desjardins@cornell.edu

Original Manuscript Submitted: 4/21/2013; Final Draft Received: 9/10/2013

A detailed understanding of the driving mechanisms behind primary atomization is crucial to the optimization of sprays for efficient combustion in modern propulsion systems. Many challenges are associated with simulating realistic turbulent atomization, such as the multiplicity of length and time scales of the turbulent flow field and gas-liquid interface, discontinuous fluid properties and pressure at the phase interface, high density ratios that degrade numerical robustness, and complex shapes of spray injectors. These challenges have hindered progress in computational modeling of atomizing two-phase flows, and as a result a complete characterization of all physical processes involved in turbulent atomization has remained elusive. This paper presents a suite of computational tools that have been developed in an effort to simulate primary atomization from first principles. The incompressible Navier-Stokes equations are handled in the context of a high-order accurate, discretely conservative, finite difference solver shown to be ideally suited for direct numerical and large-eddy simulations of turbulence. A conservative level set method is used for interface capture, improved through the use of local re-initialization enabled by an efficient fast marching method. A high-density ratio correction algorithm is employed that leads to tighter coupling between mass and momentum transport. Finally, the use of immersed boundaries allows for modeling of complex geometries without requiring body-fitted meshes, eliminating time spent generating complex grids. The framework outlined herein is shown to have the ability to capture important instabilities for atomizing flows, such as Rayleigh-Plateau and Kelvin-Helmholtz instabilities. Simulations of air-assisted breakup of both planar and coaxial liquid layers are shown to agree well with theoretical and experimental results. This strategy is employed to simulate the breakup of a turbulent liquid jet under diesel conditions, the atomization of a liquid sheet issued from a pressure swirl atomizer, and finally a complete dual-orifice atomizer, leading to qualitative insights on the atomization process. Detailed parallel scaling results are also provided.

KEY WORDS: *multiphase flow, primary atomization, direct numerical simulation, large-eddy simulation, interface capture, conservative level set, immersed boundaries*

1. INTRODUCTION

In the context of the current energy and environmental crisis, the design objectives of combustion systems are being redefined to put a stronger emphasis on reducing pollutant emissions and improving efficiency in order to reduce fuel consumption. In air-breathing, liquid-fueled combustion devices, the fuel injection process plays a fundamental role in the combustion sequence. By controlling both the diameter distribution and the spatial dispersion of fuel droplets, fuel injection directly impacts evaporation and mixing rates, and therefore is key to the quality of the subsequent combustion process. In order to optimize a process as complex as turbulent fuel injection, validated reduced-order models of primary atomization are necessary. However, such models have remained elusive, in particular due to the lack of a comprehensive theory of atomization. This lack of theoretical understanding of primary atomization is in turn easily explained by the paucity of near-injector experimental data, as liquid droplets form an optically opaque zone that surrounds the liquid core, where atomization takes place. Recently, X-ray techniques have been used to probe the details of the near-field region, see for example the work of Wang et al. (2008). While promising, this experimental technique has remained limited in its applicability, in parts due to the complexity of integrating a pressurized injection chamber inside X-ray facilities, and also due to the limited availability of often expensive X-ray technology to the broader engineering community. Consequently, it is clear that high-fidelity, detailed numerical simulations based on first principles bear the greatest potential for advancing the science of primary atomization. Generating high-quality four-dimensional (three spatial dimensions and time) atomization datasets as close as possible to relevant parameters and availing to the scientific community can have a great impact. In addition to providing much-needed insights into the physics of atomization, such datasets can also serve as the foundational reference for reduced-order model development.

A number of strategies can be employed to achieve efficient atomization in technical devices (Lefebvre, 1989). In particular, two strategies are often encountered: either the liquid is accelerated to high velocities in a near-quiescent gas, or the liquid fuel is injected at low speeds with a coflow of high-speed gas. In the first case, commonly referred to as pressurized injection, the liquid carries most of the momentum, while in the second case, commonly referred to as air-assisted injection, the gas carries most of the momentum. In both cases, the flow is highly unsteady and turbulent, and involves complex injector geometries. The vast disparity of length and time scales present in a multiphase turbulent environment leads to high-resolution requirements, as computational domains must be large enough to resolve the most energetic scales on the order of the injector inlet diameter, while also providing sufficient resolution to capture the smallest drops important to efficient combustion. The continued progression of high-performance computing is pushing current computational feasibility closer and closer to attaining the necessary computing power to completely resolve full-scale injectors. However, while direct numerical simulations (DNS) at conditions approaching that of realistic injectors have been performed in two (Boeck et al., 2006; Fuster et al., 2009) and three dimensions (Agbaglah et al., 2011; Desjardins and Moureau, 2010; Desjardins et al., 2008; Desjardins and Pitsch, 2009; Fuster et al., 2009; Lebas et al., 2009; Menard et al., 2005; Sander and Weigang, 2008), routine use of DNS at realistic conditions is still beyond the reach of most of today's computing clusters. While requiring physical models for the smallest scales of the flow, about which little is known, large-eddy simulation (LES) has been shown to be a useful tool that can provide much more flexibility on resolution while still capturing most of the dynamic processes that govern primary atomization. This approach has been shown to be useful in a variety of applications related to atomization and spray formation (Rayana, 2007; Herrmann, 2010; Ménard et al., 2007; Jones and Lettieri, 2010; Moin, 2004; Oefelein, 2006; Pitsch et al., 2008; Villiers et al., 2004; Vuorinen et al., 2010).

Liquid-gas flow simulations require special treatment of the phase interface, as the immiscibility of the phases and the singular nature of the surface tension force lead to discontinuities in fluid properties and pressure. These discontinuities lead to numerical oscillations and low orders of convergence if not accounted for in an appropriate fashion. One approach proposed by Brackbill et al. (1992), known as the continuum surface force model (CSF), is to smear out discontinuities to make them continuous over a length scale resolvable by the mesh. Another approach, the ghost fluid method (GFM) of Fedkiw et al. (1999), accounts for the jump conditions through the use of Taylor series expansions, explicitly modifying the discretization of the pressure-Poisson equation. This approach can be seen as a natural extension of finite difference discretization for discontinuous variables, and is true to the discontinuous nature of liquid-gas flows, at least to first-order accuracy. Both the GFM and the CSF strategies require the knowledge of the location of the interface, which evolves through material transport. Level set methods (Osher and Sethian, 1988) provide a means for transporting a phase interface by implicitly defining the interface as an isolevel of a smooth auxiliary function, leading to a variety of desirable properties, including automatic handling of topology changes and convenient calculation of interfacial curvature. This implicit definition is very convenient compared to the geometric representation of the interface in volume of fluid (VOF) methods (Hirt and Nichols, 1981), which require interface reconstruction from cell volume fractions by way of simple-line interface calculation (SLIC) (Noh and Woodward, 1976) or piecewise linear interface calculation (PLIC) (Parker and Youngs, 1992), for example. However, in contrast to level set methods, VOF methods tend to be discretely conservative. Certain multiphase applications can also require the extrapolation of data across the interface (Fedkiw et al., 1999; Aslam, 2001; van Poppel et al., 2010), which has been done by solving a Hamilton-Jacobi-type equation in a variety of level set applications (Fedkiw et al., 1999; Chen et al., 1994; Fedkiw et al., 1999; Losasso et al., 2006; Peng et al., 1999; Sussman et al., 1994). However, the computationally efficient fast marching method (FMM) (Adalsteinsson and Sethian, 1999;

Sethian, 1996) can also been extended to perform rapid high-order extrapolations across discontinuities.

Multiphase computations become increasingly difficult as the density ratio between the phases increases. This is due in part to the ill-conditioning of the pressure Poisson equation used to enforce the solenoidal condition for incompressible simulations. In the framework presented below, the Navier-Stokes solver NGA (Desjardins et al., 2008) utilizes a black-box multigrid solver (BBMG) (Dendy, 1982) as a robust preconditioner of a conjugate gradient solver (Van der Vorst, 1986; Van der Vorst and Dekker, 1988) to maintain convergence regardless of the density ratio. Still, inconsistencies between mass and momentum transport can lead to spurious fluctuations in kinetic energy that are amplified by the presence of strong interfacial shear in a turbulent environment. This is alleviated here by enforcing a discrete consistency condition between the mass flux associated with the interface transport and the momentum flux used in the Navier-Stokes solver. This idea, first introduced in the context of VOF schemes (Rudman, 1998), was adapted to level set methods (Desjardins and Moureau, 2010), and is used here with the accurate conservative level set method (Desjardins et al., 2008).

The complex geometries associated with injection systems also require special consideration. Using a body-fitted mesh can be challenging due to the sheer cost of mesh generation. An alternative approach is to model the effect of the geometry using an immersed boundary method (Mittal and Iaccarino, 2005), a technique that modifies the operators of computational cells that are cut by the boundary to account for embedded boundary conditions. This approach allows for the use of Cartesian meshes, benefiting from the simplicity and speed of the algorithms corresponding to their structured nature.

The governing equations solved in the current study are presented in Sec. 2, followed by a discussion of the various numerical aspects of the computational framework in Sec. 3. Demonstration of the ability of the approach to capture instabilities relevant to atomization is then provided in Sec. 4, followed by comparison with theoretical and experimental results of planar and coaxial air-blast injection simulations in Sec. 5 and Sec. 6, respectively. Section 7 shows simulation results for primary atomization of diesel-like injection, including detailed performance analysis of the code. Finally, simulation results for primary atomization in the context of complex geometries are presented. Results for a realistic pressure swirl injector and a dual orifice air-blast injector are discussed in Sec. 8.

2. MATHEMATICAL FORMULATION

Liquid-gas flows relevant to low Mach number primary atomization are governed by the incompressible Navier-Stokes equations. For a solenoidal velocity field **u**, the continuity equation is written as

$$\frac{\partial \rho}{\partial t} + \mathbf{u} \cdot \nabla \rho = 0, \tag{1}$$

where ρ is the density and t is time. The Navier-Stokes equations are written as

$$\frac{\partial \rho \mathbf{u}}{\partial t} + \nabla \cdot (\rho \mathbf{u} \otimes \mathbf{u}) = -\nabla p + \nabla \cdot \left[\mu \left(\nabla \mathbf{u} + \nabla \mathbf{u}^{\mathsf{T}} \right) \right] + \rho \mathbf{g}, \tag{2}$$

where p is the pressure, **g** is acceleration due to gravity, and μ is the dynamic viscosity. The material properties are considered to be constant in each phase, with the subscripts l and g used to describe the liquid and gas, respectively. The jumps of these quantities across the interface Γ are introduced for convenience and defined as

$$[\rho]_\Gamma = \rho_l - \rho_g \text{ and } [\mu]_\Gamma = \mu_l - \mu_g. \tag{3}$$

The velocity field is continuous across Γ in the absence of phase change, i.e., $[\mathbf{u}]_\Gamma = 0$. The existence of surface tension forces, however, will lead to discontinuous normal stresses at the phase interface. This results in an interfacial jump in pressure, expressed as

$$[p]_\Gamma = \sigma \kappa + 2 [\mu]_\Gamma \mathbf{n}^{\mathsf{T}} \cdot \nabla \mathbf{u} \cdot \mathbf{n}, \tag{4}$$

where σ is the surface tension, κ is the interfacial curvature, and **n** is the normal vector at the interface.

3. COMPUTATIONAL FRAMEWORK

3.1 Accurate Conservative Level Set Approach

The conservative level set approach (Desjardins et al., 2008; Olsson and Kreiss, 2005; Olsson et al., 2007) defines the phase interface to be the $\psi = 0.5$ isosurface of a hyperbolic tangent level set function ψ defined by

$$\psi(\mathbf{x}, t) = \frac{1}{2} \left\{ \tanh \left[\frac{\phi(\mathbf{x}, t)}{2\varepsilon} \right] + 1 \right\}, \tag{5}$$

where ϕ is the classical signed distance level set function, defined by $\phi(\mathbf{x}, t) = \pm \|\mathbf{x} - \mathbf{x}_\Gamma\|$ where $\mathbf{x}_\Gamma$ is the location on the interface Γ that provides the minimum Euclidean distance from location **x**, and the sign reflects on which side of the interface **x** is located. The parameter ε controls the thickness of the profile and is classically chosen to be $\varepsilon = \Delta \mathbf{x}/2$, where $\Delta \mathbf{x}$ is the mesh size. The level set is transported via the material evolution equation

$$\frac{\partial \psi}{\partial t} + \mathbf{u} \cdot \nabla \psi = 0. \tag{6}$$

In the presence of a solenoidal velocity field, Eq. (6) is rewritten as

$$\frac{\partial \psi}{\partial t} + \nabla \cdot (\mathbf{u} \psi) = 0, \tag{7}$$

allowing for discretely conservative transport of ψ. Re-initialization is used to restore ψ to a hyperbolic tangent profile after transport. This is done to improve numerical robustness and conservation of the volume under the $\psi = 0.5$ isosurface. The profile in Eq. (5) is compatible with the steady-state solution of

$$\frac{\partial \psi}{\partial \tau} = \nabla \cdot \left\{ \left[\varepsilon (\nabla \psi \cdot \mathbf{n}) - \psi (1 - \psi) \right] \mathbf{n} \right\}, \tag{8}$$

where τ is a pseudo-time coordinate. Solving Eqs. (7) and (8) successively allows for advection of the interface by the fluid velocity, preserves the hyperbolic tangent profile of ψ, and maintains discrete conservation of ψ over the computational domain.

The normal vector $\mathbf{n}$ is computed from the signed distance function ϕ before the reinitialization step using

$$\mathbf{n} = \frac{\nabla \phi}{\|\nabla \phi\|} \tag{9}$$

and is kept constant during the solution of Eq. (8). To complete the algorithm, the signed distance function ϕ is obtained from the hyperbolic tangent level set function ψ using a parallel fast marching method (FMM) (Sethian, 1996, 1999; Adalsteinsson and Sethian, 1999; Herrmann, 2003). More details on the finite difference discretization of these equations can be found in Desjardins et al. (2008), and an alternate discontinuous Galerkin discretization is presented in Owkes and Desjardins (2013).

3.2 Localized Conservative Reinitialization

Excessive reinitialization has been shown to degrade computational results by compounding errors for level sets that are not perturbed by the velocity field (McCaslin and Desjardins, 2013). Thus, it is advantageous to allow for the amount of re-initialization to vary in space. To accommodate this while maintaining discrete conservation of ψ, a spatially and temporally varying factor $\alpha(\mathbf{x,t})$ is introduced into Eq. (8) to yield

$$\frac{\partial \psi}{\partial \tau} = \nabla \cdot \left\{ \alpha \left[\varepsilon (\nabla \psi \cdot \mathbf{n}) - \psi (1 - \psi) \right] \mathbf{n} \right\}. \tag{10}$$

The choice of α is based on estimated deformation of the level set profile (McCaslin and Desjardins, 2013). In particular, α is chosen to scale with $\nabla \mathbf{u} \cdot \mathbf{n}$ to account for deformation through numerical diffusion, and with $\mathbf{n}^{\mathsf{T}} \cdot \left(\nabla \mathbf{u} + \nabla \mathbf{u}^{\mathsf{T}} \right) \cdot \mathbf{n}$ to account for deformation through normal straining. Expanding Eq. (9) leads to

$$\frac{\partial \psi}{\partial \tau} = \alpha \nabla \cdot \left\{ \left[\varepsilon (\nabla \psi \cdot \mathbf{n}) - \psi (1 - \psi) \right] \mathbf{n} \right\} + \left\{ \left[\varepsilon (\nabla \psi \cdot \mathbf{n}) - \psi (1 - \psi) \right] \right\} \mathbf{n} \cdot \nabla \alpha, \tag{11}$$

which has the same steady-state solution as Eq. (8) provided $\mathbf{n} \cdot \nabla \alpha = 0$, in which case Eq. (11) reduces to

$$\frac{\partial\psi}{\partial\tilde{t}} = \nabla \cdot \{[\varepsilon(\nabla\psi \cdot \mathbf{n}) - \psi(1-\psi)]\,\mathbf{n}\}\,, \tag{12}$$

where $\tilde{t} = \alpha\tau$ is the localized pseudo-time.

The Eikonal equation, $\mathbf{n} \cdot \nabla\alpha = 0$, can be solved efficiently using FMM in conjunction with $\|\nabla\phi\| = 1$. Note that the framework of the accurate conservative level set method (ACLS) (Desjardins et al., 2008) already relies on a parallel fast marching solution of $\|\nabla\phi\| = 1$ in order to obtain accurate interfacial normals, so a majority of the calculations involved in solving the Eikonal equation is already being performed. The details of local re-initialization are beyond the scope of this paper, but the impact of the approach on interface topology for flows that contain both stagnant and moving regions of interface is demonstrated for a drop deforming in a vortex in Fig. 1. As shown in the figure, excessive reinitialization is performed when a global value of α is chosen and the final shape significantly departs from the exact solution. In comparison, when the amount of reinitialization is calculated locally from the velocity field the amount of reinitialization can be more precisely controlled and the reinitialization errors reduced.

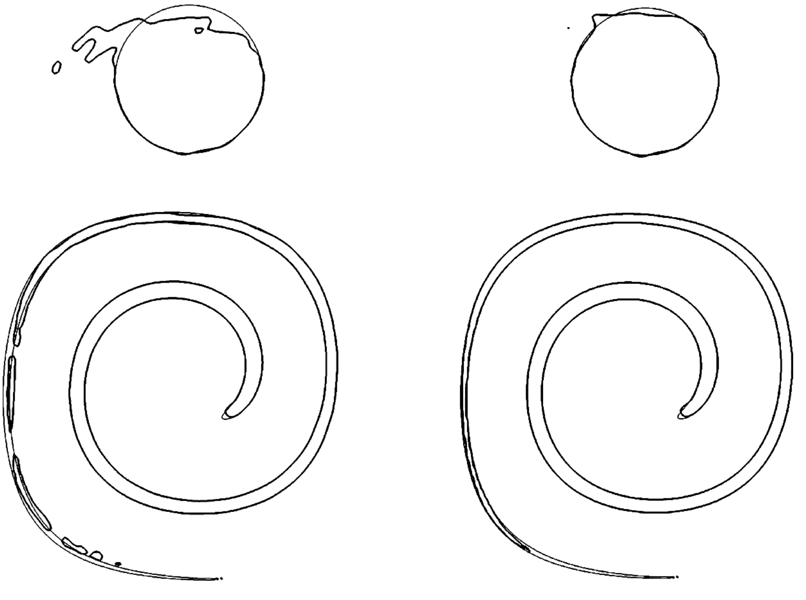

(a) (b)

FIG. 1: Effect of local re-initialization on a drop deforming in a vortex. The initial condition is shown by the thin line, overlaid by the final shape. The shape at maximum deformation is shown beneath. The test is run on a 128 × 128 mesh, and maximum deformation on a 1024 × 1024 mesh is shown for reference by the thin line: (a) Original ACLS (Desjardins et al., 2008) with global reinitialization; (b) ACLS with local re-initialization.

3.3 Consistent Mass and Momentum Fluxing

Numerical inconsistencies between the transport of mass and momentum give rise to numerical difficulties typically taking the form of spurious fluctuations in fluid momentum and kinetic energy. This problem is exacerbated by the presence of strong shear at the interface and high-density ratios, and ultimately can cause strong numerical stability issues. Note that it can affect both level set (Herrmann, 2003) and VOF methods (Scardovelli and Zaleski, 1999) since these approaches rely on very specific strategies for transporting the phase-interface, which are likely to differ from the way momentum is convected. In the context of VOF, Rudman (1997) suggested using VOF density fluxes when calculating the momentum convection term, thereby forcing a discrete compatibility between density and momentum transport. This strategy for dealing with high density ratio flows was then adapted to level set methods by Raessi (2008) and Raessi and Pitsch (2009), although their work was limited to one- and two-dimensional problems. For three-dimensional problems, a novel approach is proposed for extending this momentum flux correction to level set methods. This new high density ratio scheme performs well regardless of the density ratio and shear rate, making it ideal for air-blast fuel injection problems. We summarize this approach briefly below.

In order to advance the Navier-Stokes equations without having to deal with the discontinuous density field in the convective term, it is customary to use a form such as

$$\frac{\mathbf{u}^{\star}_{k+1}-\mathbf{u}^{n}}{\Delta t} = P_k^{n+(1/2)} - C_{k+1}^{n+(1/2)} - V_{k+1}^{n+(1/2)}, \tag{13}$$

where

$$P_k^{n+(1/2)} = -\frac{1}{\rho^{n+(1/2)}}\nabla p_k^{n+(1/2)},$$

$$C_{k+1}^{n+(1/2)} = \nabla\cdot\left(\mathbf{u}_{k+1}^{n+(1/2)}\otimes\mathbf{u}_{k+1}^{n+(1/2)}\right), \quad \text{and}$$

$$V_{k+1}^{n+(1/2)} = \frac{1}{\rho^{n+(1/2)}}\nabla\cdot\left[\mu^{n+(1/2)}\left(\nabla\mathbf{u}_{k+1}^{n+(1/2)} + \nabla\mathbf{u}_{k+1}^{n+(1/2)}\Big|^{\mathsf{T}}\right)\right]$$

are the pressure, convective, and viscous terms, respectively. The detailed implementation of these terms is described elsewhere (Desjardins et al., 2008; Desjardins and Pitsch, 2009). In these equations, the n, $n+$ (1/2), and $n+1$ superscripts represent the old time, mid-time step, and new time step, respectively. The k index refers to the subiteration number, used here in the context of an iterative Crank-Nicolson time advancement. Note that solving this equation provides $\mathbf{u}^{\star}_{k+1}$, a nonsolenoidal velocity field that needs to be corrected using the pressure Poisson equation. In order to improve the coupling between momentum convection and level set transport, the convective term is recast in conservative form that includes density, which is carefully constructed from the level set. The new convection term can be introduced in the discrete Navier-Stokes equation above in the form of a velocity update using

$$\widehat{C}_{k+1}^{n+(1/2)} = \frac{1}{\hat{\rho}^{n+1}} \nabla \cdot \left(\rho^{n+(1/2)} \mathbf{u}_{k+1}^{n+(1/2)} \otimes \mathbf{u}_{k+1}^{n+(1/2)} \right) + \frac{1}{\hat{\rho}^{n+1}} \frac{\hat{\rho}^{n+1}\mathbf{u}^n - \hat{\rho}^n \mathbf{u}^n}{\Delta t}. \quad (14)$$

In the previous expression, the density can vary by several orders of magnitude, which requires special attention. First, the density $\hat{\rho}_i^n$ in the staggered momentum cell i has to be defined, which in one dimension can be done for example by writing

$$\hat{\rho}_i^n = \rho_g + [\rho]_\Gamma \, h\left(\phi_{i-(1/2)}^n, \phi_{i+(1/2)}^n \right), \quad (15)$$

where the height fraction h is defined by

$$h\left(\phi_{i-(1/2)}^n, \phi_{i+(1/2)}^n \right) = \begin{cases} 1 \quad \text{if } \phi_{i-(1/2)}^n \geq 0 \quad \text{and} \quad \phi_{i+(1/2)}^n \geq 0 \\ 0 \quad \text{if } \phi_{i-(1/2)}^n < 0 \quad \text{and} \quad \phi_{i+(1/2)}^n < 0 \\ \dfrac{\phi_{i-(1/2)}^{n+} + \phi_{i+(1/2)}^{n+}}{|\phi_{i-(1/2)}^n| + |\phi_{i+(1/2)}^n|} \quad \text{otherwise,} \end{cases} \quad (16)$$

where $a^+ = \max(a, 0)$. Next, $\hat{\rho}^{n+(1/2)} \mathbf{u}_{k+1}^{n+(1/2)}$ is treated as a density flux for the continuity equation, discretized using a first-order upwind scheme. This leads to

$$\hat{\rho}_{i+(1/2)}^{n+(1/2)} = \begin{cases} \hat{\rho}_i^n & \text{if } \left.\mathbf{u}_{k+1}^{n+(1/2)}\right|_{i+(1/2)} \geq 0 \\ \hat{\rho}_{i+1}^n & \text{otherwise.} \end{cases} \quad (17)$$

Finally, we obtain $\hat{\rho}^{n+1}$ by solving the continuity equation on the momentum cell, leading to

$$\hat{\rho}^{n+1} = \hat{\rho}^n - \Delta t \nabla \cdot \left(\hat{\rho}^{n+(1/2)} \mathbf{u}_{k+1}^{n+(1/2)} \right). \quad (18)$$

This approach ensures a tight coupling between level set and momentum transport, since $\hat{\rho}^n$ is defined directly from the level set at each time step. While this scheme is first-order in both space and time, more accurate schemes can readily be used provided they maintain the boundedness of $\hat{\rho}^{n+1}$. Finally, note that the extension to three dimensions is straightforward.

This momentum correction scheme is evaluated on a simple two-dimensional test case of droplet transport. A droplet of diameter D is placed in the middle of a periodic computational domain of size 5D × 5D. Various meshes are considered, ranging from 32^2 to 128^2. The velocity field is initialized by giving the liquid a velocity $u_l = 1$ and $v_l = 0$, while the gas is initially at rest. The time-step size is chosen such that the convective Courant-Friedrichs-Lewy (CFL) Number remains below 0.2. Both gas and liquid viscosities, as well as the surface tension coefficient, are set to zero. Finally, the density ratio between the liquid and the gas is set to 10^6. Under these conditions, the droplet is expected to remain circular. However, the non-corrected scheme becomes unstable and fails in less than a third of a flow-through time regardless of the mesh refinement or time-step size. In comparison, the density-corrected scheme runs robustly with all meshes for any number of flow-through times. Some deformation of the drop is visible, although it does not appear to increase significantly with time. Figure 2 shows the phase interface after one flow-through time for the various meshes, compared to the exact solution. The drop shape converges satisfactorily toward the exact solution as the mesh is refined.

3.4 Pressure Poisson Equation

The pressure term comprises a jump in density and the surface tension force across the interface, hence it requires special numerical handling. To that end, the GFM (Fedkiw et al., 1999) is employed here. By formulating generalized Taylor series expansions that includes variable discontinuities, it allows the use of classical discretization strategies while maintaining the sharp nature of the discontinuities.

In one dimension, for an interface Γ located at x_Γ between x_i and x_{i+1}, where x_{i+1} is in the liquid and both x_{i-1} and x_i are in the gas, we can express the pressure gradient in the gas at $x_{i+(1/2)}$ as

$$\left.\frac{1}{\rho}\frac{\partial P}{\partial x}\right|_{g,i+(1/2)} = \frac{1}{\rho^\star}\frac{p_{l,i+1}-p_{g,i}}{\Delta x} - \frac{1}{\rho^\star}\frac{[p]_\Gamma}{\Delta x}, \tag{19}$$

where $\rho^\star = \theta\rho_g + (1-\theta)\rho_l$ is a modified density, and $\theta = (x_\Gamma - x_i)\,/\,(x_{i+1}-x_i)$ represents the fraction of the cell inside the gas. Similarly, the pressure Laplacian can be written at x_i as

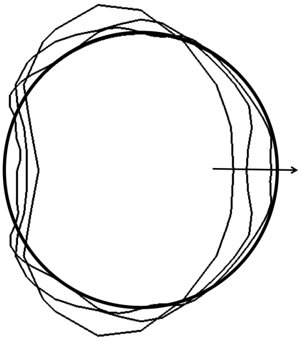

FIG. 2: Droplet shape after one flow-through time using the density-based momentum flux correction scheme. The arrow indicates mesh size increasing from 32^2 to 64^2 to 128^2, and the thick line is the exact solution.

$$\frac{\partial}{\partial x}\left(\frac{1}{\rho}\frac{\partial P}{\partial x}\right)\bigg|_{g,i} = \frac{\frac{1}{\rho^\star}\left(p_{l,i+1} - p_{g,i}\right) - \frac{1}{\rho_g}\left(p_{g,i} - p_{g,i-1}\right)}{\Delta x^2} - \frac{[p]_\Gamma}{\rho^\star \Delta x^2}. \tag{20}$$

More details on the derivation of the GFM are provided in (Fedkiw et al., 1999; Kang et al., 2000), and the derivation of Eqs. (19) and (20) is given in Desjardins et al. (2008).

Because it represents such a large part of the computational effort, an efficient and robust Poisson solver is a critical component of the computational strategy. Indeed, it is typical for the Poisson solver to account for 60% or more of the time spent per time step. In the context of multiphase flows, the presence of the density in the pressure Poisson equation leads to highly discontinuous coefficients. Recently, MacLachlan et al. (2008) investigated the performance of various Poisson solvers in the context of multiphase flows with large density ratios. Their investigation covered several solvers, including Krylov-based solvers such as preconditioned conjugate gradient, deflated conjugate gradient, and multigrid solvers such as algebraic, geometric, and matrix-based multigrid. Their study concluded that for the test problems they considered, the black-box multigrid (BBMG) solver of Dendy (1986) is the most robust and efficient method. For this reason, the choice was made to implement a BBMG solver in NGA.

The implementation follows the three-dimensional description introduced by Dendy (1983, 1986), and includes additional treatment for periodic boundary conditions proposed later (Dendy, 1988). In addition, the improvement to the original BBMG algorithm proposed by Shapira (2008) has also been used. This modification has been shown to improve convergence significantly in certain pathological cases. The relaxation step consists of an 8-color Gauss-Seidel, which is most natural to parallelize with 27-points stencils in three dimensions. The finest grid level is partitioned using the same domain decomposition strategy as in NGA, and the domain decomposition of coarser grid levels simply follows from the finest decomposition. Finally, the BBMG was introduced as a preconditioner to a conjugate gradient solver (Van der Vorst, 1986; Van der Vorst and Dekker, 1988).

3.5 Conservative Immersed Boundary

Generating boundary fitted grids to simulate flows with complex physical geometries can be an arduous process requiring the investment of a significant portion of the man-hours allocated to a given engineering project. The immersed boundary (IB) approach circumvents this problem by overlaying a complex geometry with a simple (i.e., typically Cartesian) mesh. The complex geometry is now “immersed” in the computational cells and its impact on the flow field must be modeled. Using an immersed boundary scheme, the mesh generation time is essentially reduced to zero. A wide variety of such schemes exists, differentiated by the manner in which the impact of the IB is modeled in the governing equations. The interested reader is directed to the review article of Mittal et al. (2005) for a discussion of the advantages and disadvantages of various approaches.

The cut-cell method of Meyer et al. (2010) forms the basis of the present scheme. The cut-cell methodology was chosen because it provides a sharp IB representation as well as discrete conservation of mass and momentum, making it well suited for investigation of atomization in realistic geometries.

Instead of the full Navier-Stokes equations, consider a generalized conservative transport equation for a quantity ζ given by

$$\frac{\partial \zeta}{\partial t} + \nabla \cdot \mathbf{F}(\zeta) = 0 \tag{21}$$

where t is time, and $\mathbf{F}(\zeta)$ represents the flux of ζ, possibly a diffusive, viscous, or advective flux. A typical second-order finite volume discretization of this equation leads to the following form:

$$\zeta_c^{n+1} = \zeta_c^n - \frac{\Delta t}{V_c} \sum_{f=1}^{N_{\text{faces}}} \left(A_f \overline{\mathbf{F}}_f^{\mathbf{n}+(1/2)} \cdot \mathbf{n}_f \right), \tag{22}$$

where ζ_c^n represents the cell-average value of ζ at time t^n, Δt is the time step size, V_c is the cell volume, A_f is the face area, $\mathbf{n}_f$ is the face outward normal, and $\overline{\mathbf{F}}_f$ represents the face-average flux. The presence of the IB leads to many instances where cells are cut by the fluid-solid interface, as illustrated by Fig. 3. In that case, it is appropriate to replace the cell volume V_c by the wetted volume $V_w = \alpha^V V_c$, and the face area A_f by the wetted face area $A_w = \alpha^S A_f$, which is equivalent to saying that the finite volume formulation should be obtained by integrating over the fluid part of the cell only. This leads to the following expression:

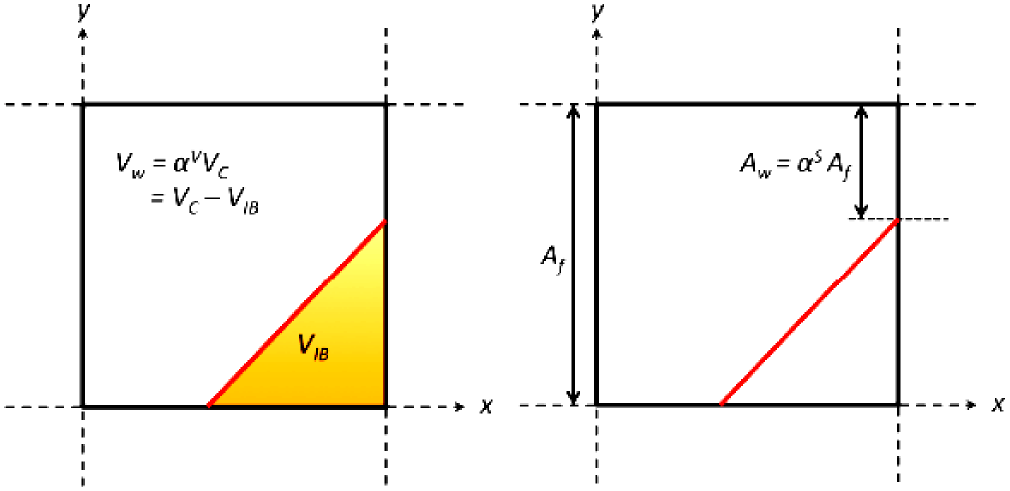

FIG. 3: Geometrical characterization of the cut cells.

$$\zeta_c^{n+1} = \zeta_c^n - \frac{\Delta t}{\alpha_c^V V_c}\left[\sum_{f=1}^{N_{\text{faces}}}\left(\alpha_f^s A_f \overline{\mathbf{F}}_f^{n+(1/2)} \cdot \mathbf{n}_f\right) + A_{\text{IB}}\overline{\mathbf{F}}_{\text{IB}}^{n+(1/2)} \cdot \mathbf{n}_{\text{IB}}\right], \tag{23}$$

where the volume and area fractions α_c and α_f are unity except in cut cells. The last term represents the flux of ζ at the IB surface, where A_{IB} is the IB area in the cell, $\mathbf{n}_{\text{IB}}$ is the outward-oriented immersed boundary normal, and $\overline{\mathbf{F}}_{\text{IB}}$ is the average flux along the IB surface in that cell.

These modifications can be conveniently implemented by modifying the divergence operators using the volume and surface fluid fractions, and adding a source term to account for any flux at the IB surface. Note that with Neumann boundary conditions, the flux through the IB surface is zero. Similarly, the convective momentum flux at a fixed non-porous surface is zero, but the viscous momentum flux is non zero.

In order to characterize the geometry of the cut-cells that are the basis of this approach, it is necessary to fully characterize the location of the immersed geometry surface. This is accomplished through the use of an implicit description in the form of an iso-surface of an additional level set function. This IB level set function, G, is chosen such that it corresponds to a standard signed distance function, i.e.,

$$|G(\mathbf{x}, t)| = \|\mathbf{x} - \mathbf{x}_{\text{IB}}\|, \tag{24}$$

where $\mathbf{x}_{\text{IB}}$ corresponds to the closest point on the solid-fluid interface from $\mathbf{x}$, and $G(\mathbf{x}, t) > 0$ on one side of the interface, and $G(\mathbf{x}, t) < 0$ on the other side. With this definition, the immersed boundary surface Γ_{IB} in a domain Ω is defined by $\Gamma_{\text{IB}}(t) = \{\mathbf{x} \in \Omega : G(\mathbf{x}, t) = 0\}$.

Once such information is made available, simple operations can be used to estimate the location of the surface, such as a linear interpolation between two points of different G sign. We then reconstruct the wetted volumes and surfaces by first decomposing each cell (assumed here to be hexahedral without loss of generality) into five simplices (tetrahedra in three dimensions), followed by a marching simplex algorithm to triangulate the interface, as illustrated in Fig. 4. Note that in three dimensions, intersecting a tetrahedron with a plane is a straightforward operation. Accounting for all possible symmetries, only three cases need to be considered: (1) no intersection, i.e., the cell is not a cut cell, (2) an intersection leaving one vertex on one side of the plane and three on the other, and (3) an intersection leaving two vertices on one side and two on the other. The result of this process is a second-order discrete representation of the cut cell in the form of a collection of tetrahedra, from which quantities such as the cut cell volume and surface areas can be readily extracted.

A critical aspect of the cut-cell methodology lies in the presence of small cells. Indeed, there is technically no limitation to how small cut cells can become. This can negatively impact the stability of the momentum solver, the conditioning of the pressure solver, and the well-posedness of the equations for certain small cells. To address

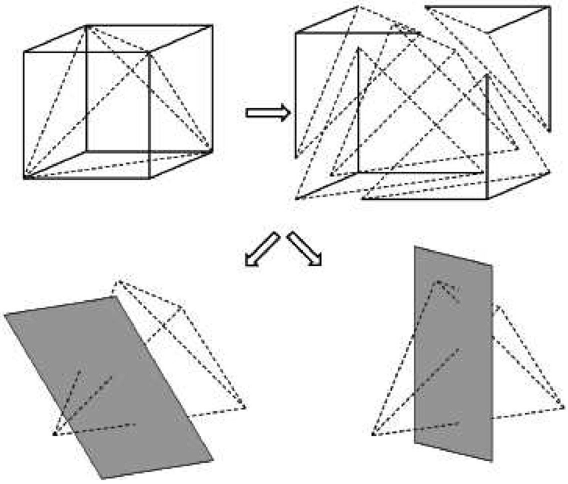

FIG. 4: Optimal decomposition of hexahedral into five simplices, followed by a marching simplex procedure to intersect the immersed surface with the cell volume.

the issue of stability, our work employs an implicit time integration based on the unconditionally stable diagonally dominant alternate direction implicit (DDADI) strategy (MacCormack, 2001). However, even with this strategy, the nonlinear convective fluxes in small cells can potentially be destabilizing. In well-resolved DNS-type simulations, it was found that due to the no-slip condition imposed at the IB, the viscous flux was typically dominant in these small cells, preventing the convective fluxes from negatively impacting stability. However, in simulating high Reynolds number flows using LES with complex geometries and coarse meshes, it was found that the viscous fluxes in the small cells were no longer sufficient to ensure stability. In these situations it is desirable to effectively tie the evolution of a small cell to that of its larger neighbors. Taking advantage of the unconditional stability of the DDADI solver, the viscous momentum flux at the face of small cells is increased until it dominates the convective flux. This implicit viscous flux-based “linking” ties the time evolution of the small cells to that of their larger neighbors in a simple, discretely conservative and unconditionally stable manner, thereby alleviating all CFL constraints imposed by the small cells.

Whereas small momentum cells can cause severe time-step restrictions as mentioned above, small pressure cells can lead to a very poorly conditioned Poisson system for the pressure. To address this issue, we send the geometric information of small pressure cells (such as volume and area fractions) to their neighbors and remove the small pressure cells.

The final numerical difficulty occurs when a momentum cell does not have a well-defined pressure gradient due to one of the pressure cells being fully inside the IB. These cells will generally be small and dominated by viscous flux due to the presence of the

IB. Thus, the velocity in these cells is simply set to that of the IB, as this is compatible with what a more accurately computed viscous flux would do in these cells.

Compared with other cut-cell methods (Meyer et al., 2010; Kirkpatrick et al., 2003; Hartmann et al., 2011), the present method is surprisingly simple. The divergence operators are rescaled according to the geometry of the IB followed by three straightforward fixes: (1) adjusting the face viscosity at a few small cells, (2) adjusting the geometry of certain small pressure cells, and (3) overwriting the momentum in cells for which the Navier-Stokes equations cannot be solved. Following the procedure in Brady et al. (2012), this scheme has been verified using the method of manufactured solutions. Second-order convergence was achieved in the L_2 and L_∞ norms for velocity. For the pressure, second-order convergence was achieved in the L_2 norm, with better than first-order convergence in L_∞.

3.6 Large-Eddy Simulation Strategy

In the large-eddy simulation (LES) framework, only features existing on length scales larger than a specified value are resolved, and all smaller scales are modeled. This length scale is determined by the filtering operation

$$\tilde{f}(\mathbf{x},t) = \int_\Omega \mathcal{F}(\mathbf{x}-\mathbf{x}')\, f(\mathbf{x}',t)\, d\mathbf{x}'\,, \tag{25}$$

where $\tilde{f}$ is an arbitrary spatially-filtered quantity, Ω denotes the integration domain, and the spatial filter function $\mathcal{F}$ can be simply defined as

$$\mathcal{F}(\mathbf{x}-\mathbf{x}') = \begin{cases} 1 & \text{if } \|\mathbf{x}-\mathbf{x}'\| \le \dfrac{\Delta}{2} \\ 0 & \text{otherwise} \end{cases} \tag{26}$$

for a given filter size Δ, which is typically determined by the mesh. In this work, the filtered equations are written in each phase independently, and the effect of filtering variable fluid properties is neglected. The filtered Navier-Stokes equation within each phase yields

$$\frac{\partial \tilde{\mathbf{u}}}{\partial t} + \nabla\cdot\left(\widetilde{\mathbf{u}\otimes\mathbf{u}}\right) = -\frac{1}{\rho}\nabla\tilde{p} + \nabla\cdot\left(\mu\left[\nabla\tilde{\mathbf{u}} + \nabla\tilde{\mathbf{u}}^{\mathsf{T}}\right]\right) + \mathbf{g}, \tag{27}$$

where ρ and ν are, respectively, the density and kinematic viscosity of the phase the equation is written for. The term $\widetilde{\mathbf{u}\otimes\mathbf{u}}$ that arises from filtering the nonlinear term is closed with eddy viscosity-type models, written as

$$\widetilde{\mathbf{u}\otimes\mathbf{u}} = \tilde{\mathbf{u}}\otimes\tilde{\mathbf{u}} - 2\nu_t\tilde{\mathbf{S}}\,, \tag{28}$$

where $\tilde{\mathbf{S}} = (\nabla\tilde{\mathbf{u}} + \nabla\tilde{\mathbf{u}}^{\mathsf{T}})/2$ is the symmetric portion of the filtered velocity gradient tensor, and ν_t is the subgrid kinematic eddy viscosity. The Lagrangian dynamic subgrid scale model of Meneveau et al. (1996) is used in this work in order to calculate ν_t. Clearly, this LES formalism is incomplete for turbulent atomizing two-phase flows, since the effect of filtering variables across the phase interface is ignored.

4. COMPUTATION OF INTERFACIAL INSTABILITIES

Interfacial instabilities play important destabilizing roles for liquid atomization. Two such instabilities are the Kelvin-Helmholtz instability and the Rayleigh-Plateau instability. This section displays the ability of the NGA framework to capture these important interfacial dynamics.

4.1 Kelvin-Helmholtz Instability

The Kelvin-Helmholtz (KH) instability is a shear instability that plays a predominant role in the early destabilization mechanism for liquid jets. Proper simulation of the KH instability is crucial to accurate predictions of primary atomization. Using the computational framework described above, the KH instability was simulated with the four different sets of conditions provided in Table 1 (Owkes and Desjardins, 2013).

A schematic of the setup is shown in Fig. 5. The Reynolds and Weber numbers for the gas and liquid are

$$\begin{aligned} \mathrm{Re}_g &= \frac{\rho_g U \delta}{\mu_g}, \quad \mathrm{Re}_l = \frac{\rho_l U \delta}{\mu_l}, \\ \mathrm{We}_g &= \frac{\rho_g U^2 \delta}{\sigma}, \quad \mathrm{We}_l = \frac{\rho_l U^2 \delta}{\sigma}, \end{aligned} \tag{29}$$

where U is the velocity of the gas away from the interface and δ is the vorticity thickness of the velocity profile, taken to be $\delta = \delta_g$. Further details of the rather involved solution procedure are provided by Owkes and Desjardins (2013). Results from the study are

TABLE 1: Four cases in the KH instability simulations of Owkes and Desjardins (2013)

Case	ρ_l/ρ_g	μ_l/μ_g	$\mathbf{Re}_g$	$\mathbf{Re}_l$	$\mathbf{We}_g$	$\mathbf{We}_l$
A	10	1	2000	200	∞	∞
B	10	1	2000	200	10	10
C	1.01	10	2000	19,800	∞	∞
D	1.01	10	2000	19,800	10	10

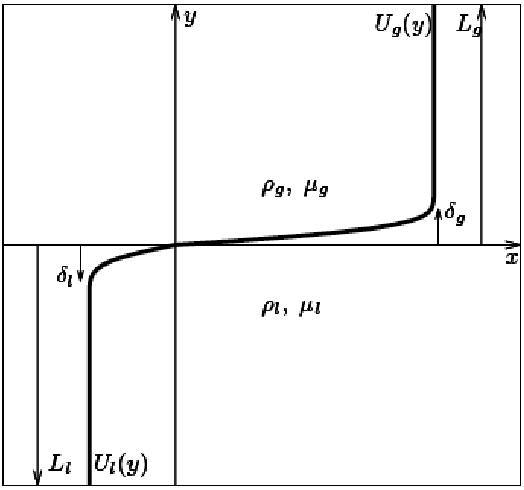

FIG. 5: Geometry used for Kelvin-Helmholtz test case. Gas is located in the top half of the domain and liquid in the bottom. The liquid and gas boundary layer thicknesses, δ_l and δ_g, are shown along with the distance from the interface to the top and bottom of the domain represented by L_g and L_l, respectively. The parallel base flow profile is depicted and labeled $U_g(y)$ in the gas and $U_l(y)$ in the liquid.

provided in Fig. 6 and show the nondimensional growth rate $\kappa c_i \delta / U$ as a function of the nondimensional wavenumber $\kappa\delta$. For all of the cases, the simulations predict the most unstable wavenumber well, even on coarse meshes with as few as eight cells per wavelength. As the mesh is refined, the solution converges toward the theoretical solution, suggesting the computational framework is fully capable of capturing the KH instability.

4.2 Rayleigh-Plateau Instability

Surface tension often plays a stabilizing role in multiphase flow phenomena, for example in parallel shear flows or for an interface subject to gravitational destabilization in Rayleigh-Taylor-type configurations. The Rayleigh-Plateau instability is an interesting instance in which surface tension actually acts to destabilize an interface. Interplay between local curvature and pressure along elongated structures gives rise to capillary wave amplification and the eventual pinch-off of a liquid column into droplets.

Rayleigh-Plateau is an important mechanism in the disintegration of ligaments into droplets, and it is therefore important to ensure the capability of the proposed framework to reproduce theoretical results. A schematic of the simulations setup is depicted in Fig. 7(a) and shows a ligament perturbed by an interfacial instability. Simulation details are provided by Desjardins et al. (2008), and only the results for nondimensional

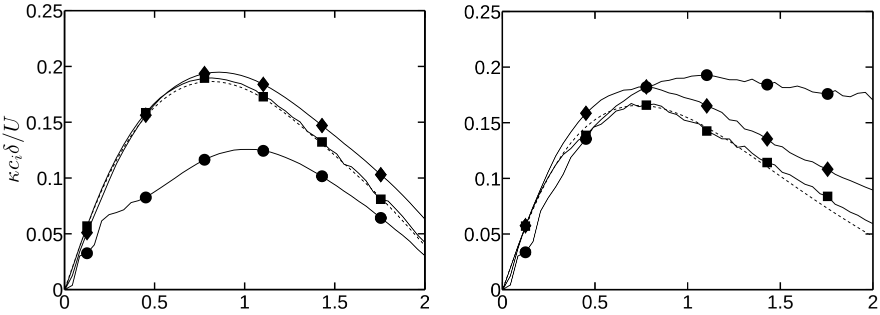

(a) Case A

(b) Case B

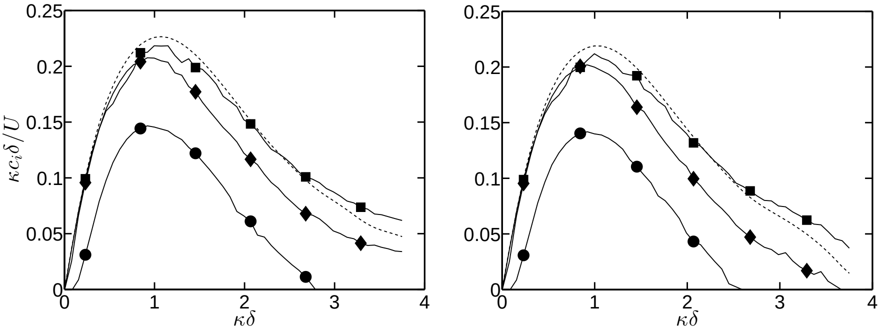

(c) Case C

(d) Case D

FIG. 6: Computed and theoretical growth rates for the four sets of conditions in Table 1. Three different meshes were used: 8 × 8 (●), 32 × 32 (◆), 128 × 128 (■). The theoretical solution is shown by the dotted line.

growth rate β/β_0 as a function of nondimensional wavenumber $\xi = 2\pi r_0/\lambda$ are recapitulated in Fig. 7(b), where $\beta = \sqrt{\sigma/(\rho_l r^3)}$ is the growth rate, r is the radius of the column, $r_0 = 0.33 \times 10^{-3}$ is the unperturbed column radius, $\beta_0 = \sqrt{\sigma/\left(\rho_l r_0^3\right)}$ is used to normalize the growth rate, and the initial perturbation wavelength is λ. These results, obtained with only 24 cells per ligament diameter, demonstrate a very satisfactory ability of the method to capture the capillary instability.

5. AIR-ASSISTED ATOMIZATION OF A LIQUID LAYER

5.1 Problem Description

Planar shear layers provide a simplified framework to study the shear instability present in realistic coaxial air-blast injectors of propulsion devices. The air-assisted atomization scenario is characterized by a high-speed gas coflowing with a low-speed liquid,

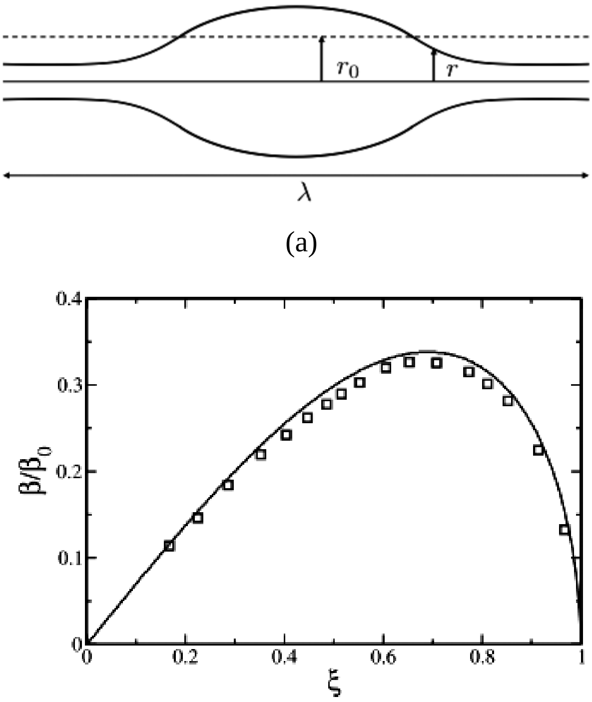

(a)

(b)

FIG. 7: Rayleigh-Plateau instability: (a) Schematic illustrating the setup for the Rayleigh-Plateau instability simulation; (b) Growth rate of the disturbance as a function of its wavelength for the capillary instability. Simulation with 24 points in the radial direction (symbols), and linear theory by Weber (1931) (line).

leading to large dynamic pressure ratios and density ratios. The air-water configuration considered was studied experimentally by Raynal et al. (1997) and is shown in Fig. 8.

The axial instability for the configuration shown in Fig. 8 that leads to the initial formation of waves is of a KH type, followed by further destabilization in the transverse direction through an instability akin to Rayleigh-Taylor. Although the transverse instability is not accounted for in the present two-dimensional (2D) simulations, both the initial shear instability and the formation of a potential liquid cone are inherently 2D and can therefore be captured within the framework of the current study. Though similar in nature to KH, the resulting most amplified wavelength and growth rate of the instability differ from the classical potential flow analysis due to the continuous nature of the velocity profile across the interface, i.e., a finite vorticity thickness δ across the interface. The planar liquid-gas shear layer experiments of Raynal et al. (1997) and the scaling arguments of Villermaux (1998) suggested that

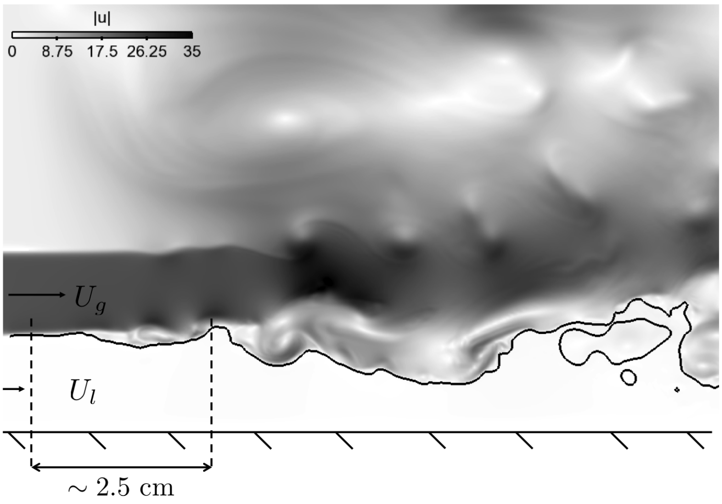

(a) M = 4

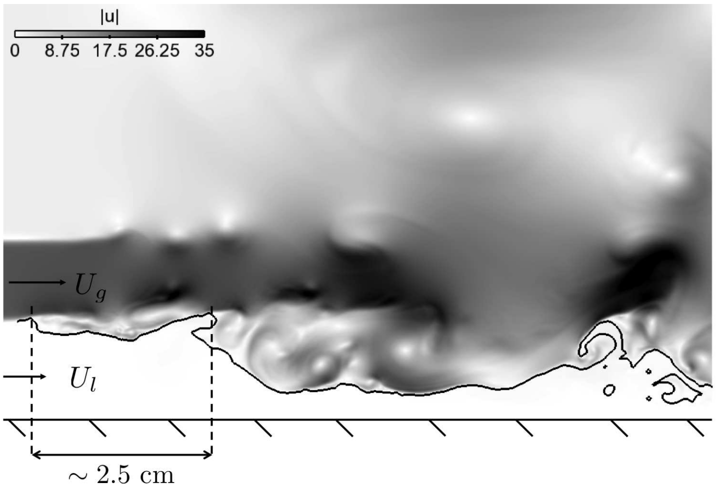

(b) M = 16

FIG. 8: Instantaneous results of the assisted atomization simulations. Colors indicate velocity magnitude, ranging from 0 (white) to 35 m/s (black). The solid black line gives the phase interface location.

$$\lambda_{\text{axi}} \sim \delta \left(\frac{\rho_l}{\rho_g} \right)^{1/2}, \tag{30}$$

where λ_{axi} is the most unstable wavelength of the shear instability. Using coaxial injectors, Marmottant and Villermaux (2004) confirmed through measurements that

$$\lambda_{\text{axi}} = c\delta \left(\frac{\rho_l}{\rho_g} \right)^{1/2} , \tag{31}$$

with the proportionality constant c varying between 1.0 and 1.4. The planar injection experiments of Rayana et al. (2006) obtained values of c in the range of 1.5–1.8. Inviscid stability analysis predicts $c = 4.2$, and the discrepancy potentially lies in both the finite vorticity thickness and the fact that the effective δ is slightly altered by the finite width of the injector tip.

5.2 Simulation Parameters

The Navier-Stokes solver NGA (Desjardins et al., 2008) is coupled to the interface capture scheme to perform an LES of the assisted atomization problem. The LES aims to match the parameters of the experiment performed by Rayana et al. (2006). Snapshots of the results for two simulations at different momentum flux ratio M are depicted in Fig. 8. The liquid layer of thickness H_l and bulk velocity U_l is separated from the gas layer of thickness H_g and bulk velocity U_g by a splitter plate of thickness θ. The vorticity thickness of the gas stream varies as a laminar boundary layer, i.e, inversely with the square root of the gas Reynolds number $Re_g = U_g H_g / \nu_g$, and Rayana et al. (2006) measured δ as

$$\delta = \frac{6H_g}{\text{Re}_g^{1/2}} \tag{32}$$

for all H_g and Re_g. To best represent the experimental conditions, the inflow velocity profiles in the simulation for each phase are specified as

$$u_{l,g}(y) = \widetilde{U}_{l,g} \tanh\left(\frac{y}{\delta}\right) , \tag{33}$$

where $\widetilde{U}_{l,g}$ are determined such that

$$\frac{1}{H_l} \int_0^{H_l} u_l(y)\, dy = U_l, \qquad \frac{1}{H_g} \int_{H_l+\theta}^{H_l+\theta+H_g} u_g(y)\, dy = U_g. \tag{34}$$

The vertical coordinate is y, and $y = 0$ corresponds to the wall below the liquid layer. The parameters used in the two simulations are summarized in Table 2, leading to the resulting dimensionless parameters in Table 3. The Reynolds numbers are $\text{Re}_{l,g} = \rho_{l,g} U_{l,g} H_{l,g} / \mu_{l,g}$, and the Weber numbers are $\text{We}_{l,g} = \rho_{l,g} U_{l,g}^2 H_{l,g} / \sigma$.

The LES is performed on a 2D domain defined by $x \in [0, L_x]$, $L_x = 8.6$ cm and $y \in [0, L_y]$, $L_y = 4$ cm, resolved by 576 × 276 cells in the x and y directions, respectively. In the region $y \leq 3H_l$ the mesh is composed of a uniform cell size $\Delta x = \Delta y = \theta/2 = 150$ μm. For $y > 3H_l$ the mesh is stretched in the y direction with a stretching ratio of 1.01. The splitter plate is modeled by enforcing $\mathbf{u} = 0$ for the cells corresponding

TABLE 2: Dimensional parameters for the air-assisted atomization LES. Note the two values of U_l correspond to two different test cases denoted with $M = 4$ and $M = 16$, respectively

H_l (m)	0.01
H_g (m)	0.01
θ (μm)	300
U_l (m/s)	0.173, 0.346
U_g (m/s)	20
ρ_l (kg/m^3)	1000
ρ_g (kg/m^3)	1.2
σ (N/m)	0.069
μ_l (Pa $\cdot$ s)	0.001
μ_g (Pa $\cdot$ s)	0.000017

TABLE 3: Dimensionless parameters for the air-assisted atomization LES

M	**Re**$_g$	**Re**$_l$	**We**$_g$	**We**$_l$
4	14,118	1,730	70	4.3
16	14,118	3,460	70	17.4

to $H_l \leq y \leq H_l + \theta$ and $0 \leq x \leq 10\theta$. This allows the tip of the splitter plate to protrude slightly into the domain, as it was suggested by Fuster et al. (2009) that this is physically important. Neumann boundary conditions are employed at the top of the domain, the no-slip condition at the bottom, and a convective outflow condition is employed at the exit plane.

The chosen mesh resolution leads to a value of Δx that is significantly smaller than δ, allowing for sufficient resolution of the vorticity thickness and subsequent capturing of the physical process responsible for the scaling in Eq. (30). Limited testing on finer meshes with $\Delta x = 100$ μm and $\Delta x = 75$ μm showed no qualitative difference from the current mesh.

In the simulations, few liquid droplets exist and were only observed to form when wave crests rise into the gas stream and break up. This is consistent with the near-inlet region of the experiment. Note that such breakup instances are not portrayed in Fig. 8.

5.3 Analysis and Results

Estimates of statistical stationarity of the shear layer suggest that the simulation is stationary for dimensionless times $U_g t / L_x \geq 93$, i.e., on the order of 10^2 gas flow-through times. The analysis presented here is for times corresponding to 209 $\leq U_g t/L_x \leq$ 417. A global quantity of interest in the assisted atomization simulation is the length of the liquid potential cone L_c that forms when statistical stationarity is reached. This length depends on the relative strength of the aerodynamic force that the gas flow imposes on the liquid, and thus governs how much of the liquid is entrained into the high-momentum gas stream. Following the reasoning of Villermaux (1998), Rayana et al. (2006) predicted this length to depend on the dynamic pressure ratio

$$M = \frac{\rho_g U_g^2}{\rho_l U_l^2}\,, \tag{35}$$

according to the relation

$$L_c = \frac{12 H_l}{\sqrt{M}}\,. \tag{36}$$

It is clearly visible from the simulation snapshots in Fig. 8 that the amount of liquid that persists in the liquid core depends on M. Figure 9 shows instantaneous values of

$$H(x,t) = \Delta x \int_0^{L_y} V_l(x,y,t)\,dy \tag{37}$$

compared to Eq. (36), where $V_l(x,y,t)$ is the liquid volume fraction within a given computational cell. Vertically integrating this quantity provides a useful metric for interfacial topology as a function of x and t. Good agreement with the theoretical prediction is observed for both $M =$ 4 and $M =$ 16.

Information regarding the axial instability wavelength λ_{axi} is attained through proper orthogonal decomposition (POD) of the fluctuating interface height $h(x,t)$, defined as

$$h(x,t) = H(x,t) - \langle H(x,t) \rangle\,, \tag{38}$$

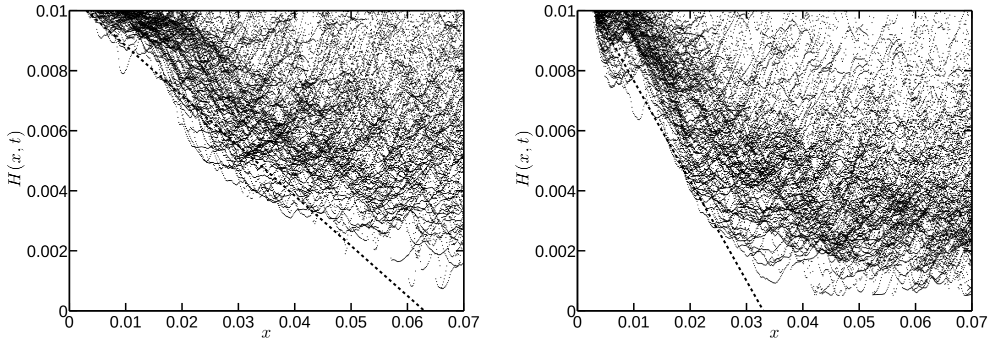

(a) $M = 4$ (b) $M = 16$

FIG. 9: $H(x,t)$ sampled over time and space (symbols) compared to Eq. (36) (dashed line).

where $\langle * \rangle$ denotes a temporal average. POD expresses $h(x,t)$ as

$$h(x,t) \approx h_r(x,t) = \sum_{k=1}^{r} a_k(t)\, b_k(x)\,, \tag{39}$$

where $r = \min(n_x, n_t)$ is the minimum between the number of spatial coordinates n_x and time samples n_t. If, for a given value of m such that $1 \leq m \leq r$, $h_m(x,t)$ is the optimal reconstruction of $h(x,t)$ in the Frobenius norm, then $b_k(x)$, k = 1, 2, . . . , m are the m proper orthogonal modes of $h(x,t)$. This approach is used to reconstruct rank-m approximations of $h(x,t)$. When modulated by the temporal coefficients a_k, the POD modes b_k most efficiently reconstruct the interface height fluctuation.

Singular value decomposition (SVD) (Kerschen et al., 2005) is used to perform the POD discretely. The first singular value corresponding to the first orthogonal mode $b_1(x)$ contains most of the interfacial topology content. This first mode is shown in Fig. 10 for $M = 4$ and $M = 16$. Estimates of the shear instability wavelength reported in Table 4 are obtained by taking the distance between the first two crests in $b_1(x)$, as indicated in Fig. 10. These values agree reasonably well with the probability density function of λ_{axi} in Fig. 11, generated by Rayana et al. (2006), noting that the PDF was generated for $M = 16$ and $\theta = 150$ μm. Due to spatial resolution, $\theta = 300$ μm is used in the simulations. The injector tip thickness θ does impact the effective vorticity thickness, and for $M = 16$ and $U_g = 20$ m/s, Rayana (2007) measured λ_{axi} for different values of θ in the ranges specified in Table 5.

6. AIR-BLAST N-DODECANE ATOMIZATION

Air-blast atomization of hydrocarbon fuels is of critical importance to the transportation sector, in particular for aircraft gas turbine engines. In this section, a co-annular air-blast n-dodecane injector is studied both experimentally and numerically. Experiments combine high-resolution and high-speed imaging of the near-field region, with global size

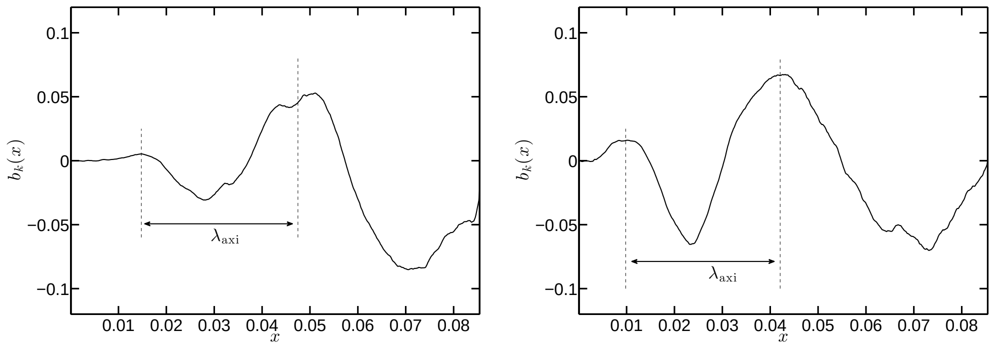

(a) M = 4 (b) M = 16

FIG. 10: Extracting the shear instability wavelength from the first POD mode.

TABLE 4: Most amplified wavelength for different M

M	λ_{axi} **[cm]**
4	3.27
16	3.23

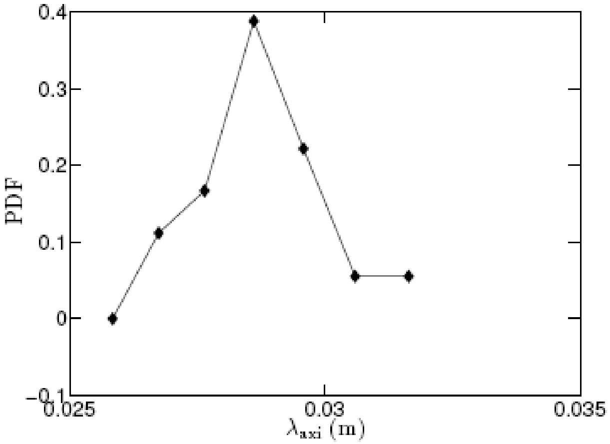

FIG. 11: PDF of λ_{axi} measured by (Rayana et al., 2006).

TABLE 5: Variation of λ_{axi} as a function of θ for $M = 16$, $U_g = 20$ m/s. Measurements done by Rayana (2007)

θ **[μm]**	λ_{axi} **[cm]**
150	2.16–2.75
450	2.25–3.3
1000	3.6–4.4
2200	3.99–4.4

and velocity (GSV) Particle Image Velocimetry (PIV) measurements of drop sizes and velocities at multiple locations downstream of the nozzle. Computational results using the proposed framework are compared to experimental measurements, showing the satisfactory behavior of the simulation technique. In particular, the onset of breakup, most unstable wavelength, and drop size and velocity distributions are in good agreement, suggesting that the fundamental physics of air-blast atomization are well captured by the simulations.

6.1 Experimental and Numerical Setup

The experimental investigation on the atomizing jet was performed by TDA Research and CU-Boulder using an external mixing air-blast atomizer as described herein. The air-blast atomizer shown in Fig. 12 was designed after the one described by Marmottant and Villermaux (2004). The simple, externally mixed geometry is well-suited for numerical modeling and code validation. The atomizer comprises two coannular tubes with fuel flow through the inner tube and nitrogen flow through the annulus between the tubes. Since transitional or developing flows are much more difficult to simulate with accuracy, the tube lengths were chosen to ensure fully developed flows at the exit.

A variety of quantities was gathered from both experiments and simulations to facilitate a validation of numerical methods. Images of the experimental jet and renderings of the simulated jet were created and examined qualitatively. Probability density functions of drop size and drop velocity were calculated to show the probability of a droplet being created of a given diameter and with a certain velocity, respectively. n-Dodecane was injected with a coflow of nitrogen; their respective properties are shown in Table 6 with the subscript l for liquid n-dodecane and g for nitrogen gas. The high-density ratio of 597 is feasible due to the consistency between mass and momentum transport described previously.

The injector geometry is detailed in Fig. 13 and consists of a straight jet of diameter d_1 surrounded by a coflow of inner diameter d_2 and thickness h. The length of the injec-

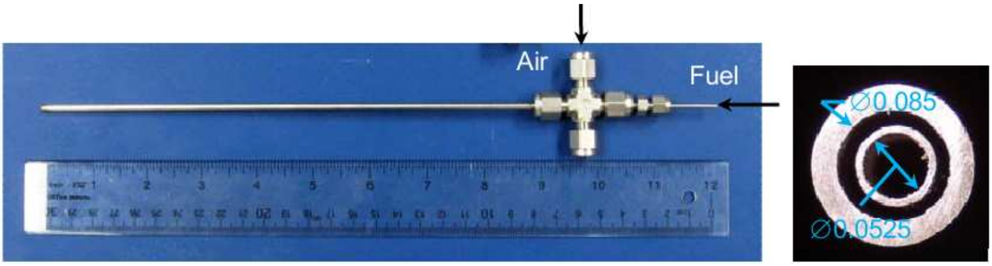

FIG. 12: Geometry of air-blast atomizer.

TABLE 6: Properties of n-dodecane and nitrogen

Density	ρ_l	746 kg/m^3
	ρ_g	1.25 kg/m^3
Surface tension	σ	2.535×10^{-2} N/m
Dynamic viscosity	μ_l	1.34×10^{-3} kg/m · s
	μ_g	1.718×10^{-5} kg/m · s

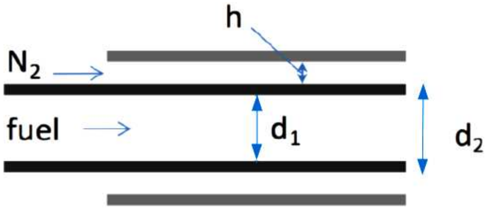

$$d_1 = 1.3335 \times 10^{-3}\ m$$
$$d_2 = 1.5875 \times 10^{-3}\ m$$
$$h = 2.8575 \times 10^{-4}\ m$$

FIG. 13: Air-blast injector dimensions.

tor is not shown in the sketch but is visible in Fig. 12 and has been designed so that the flow leaving the nozzle is fully developed.

The phase Reynolds and Weber numbers are based on the liquid velocity U_l and gas velocity U_g, and are provided in Table 7. Reynolds numbers for the test case indicate that the flow of n-dodecane and the coflow of N_2 are laminar. The laminar nature of the coflow was confirmed by numerically simulating a periodic annular pipe under similar conditions.

The atomization simulation was performed on 1024 processors using a mesh of 512 × 256 × 256 grid cells. The computational domain was $16d_1 \times 8d_1 \times 8d_1$, leading to a cell size of approximately 40 μm. A CFL number below 0.9 was maintained throughout the simulation. Roughly 1.5 flow-through times were used to allow the jet to reach a statistically stationary state.

6.2 Shear Instability Results

Primary atomization under the flow parameters described above results in an initially smooth jet that rapidly breaks up into droplets. Figure 14 shows a side-by-side comparison of snapshots from the experiment and the simulation. Qualitatively, there is excellent agreement in the shape of the jet, the length scales of instabilities, the onset of liquid breakup, and the distribution of large droplets. There appear to be smaller droplets in the experiment that are not found in the simulation result, which might indicate that the mesh should be further refined. However, it is also observed that such small droplets are often formed in the experiment when liquid accumulates on the outside of the nozzle and the jet interacts with this liquid, which does not happen in the simulation. Figure 15 shows an instance of the n-dodecane jet interacting with the wetted nozzle.

At the exit plane of the nozzle there exists a shear layer between the fast-moving coflow of gas and the slower moving liquid jet. As discussed for the planar shear layer in

TABLE 7: Flow parameters for the test case

U_l **[m/s]**	U_g **[m/s]**	**Re**$_l$	**Re**$_g$	**We**$_l$	**We**$_g$
1.8	69.89	1336	1453	127	321

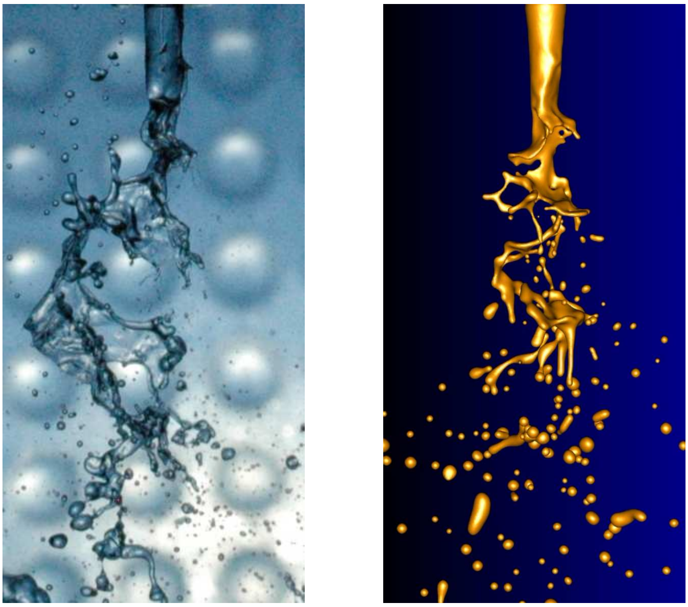

(a) Photo of experiment (b) Rendering of simulation result

FIG. 14: Comparison of jet from (a) experiment and (b) simulation.

FIG. 15: Example of nozzle wetting and the effect on breakup process.

Sec. 5, Marmottant and Villermaux (2004) showed that this flow destabilizes by means of a Kelvin-Helmholtz-type of instability, and the most amplified wavenumber is given by

$$k_m \approx 1.5 \left(\frac{\rho_g}{\rho_l} \right)^{1/2} \frac{1}{\delta}, \tag{40}$$

where δ is again the vorticity thickness of the gas jet. An *a priori* estimate of δ is challenging to obtain due to the presence of the gap between the jet and co-flow. However, to build an estimate of δ, the boundary layer thickness is defined as the location where the velocity is 50% of its maximum. Using a Poiseuille velocity profile, consistent with the laminar inflow, this approximation results in $\delta = 2.3 \times 10^{-5}$ m and $k_m = 2600$ m^{-1}. Converting from wavenumber to wavelength λ_{axi} leads to $\lambda_{\text{axi}} = 2.4 \times 10^{-3}$ m or 1.8 jet diameters ($1.8D$). Looking at Figs. 16(a) and 16(b), four different waves were identified and measured using a photo analysis program. The average wavelength was found to be $2.25D$. A similar analysis was performed for results obtained from the simulation and Fig. 16(c) shows that the average wavelength in the simulations is about $1.9D$.

In summary, the theoretical calculation predicts the wavelength to be near $1.8D$, the experiment showed $2.25D$, and $1.9D$ was found using the simulation. All of the values are of the same order of magnitude and agree reasonably well, indicating the leading breakup mechanism is an instability akin to KH. Furthermore, this analysis shows that the simulations are capable of capturing the shear layer and the effects it has on the flow.

6.3 Drop Characteristics

Drops were identified and characterized in experiments and simulations since the size of droplets produced by primary atomization is an important result for combustion-related applications. For the experiments, a TSI PIV system with the GSV option was used

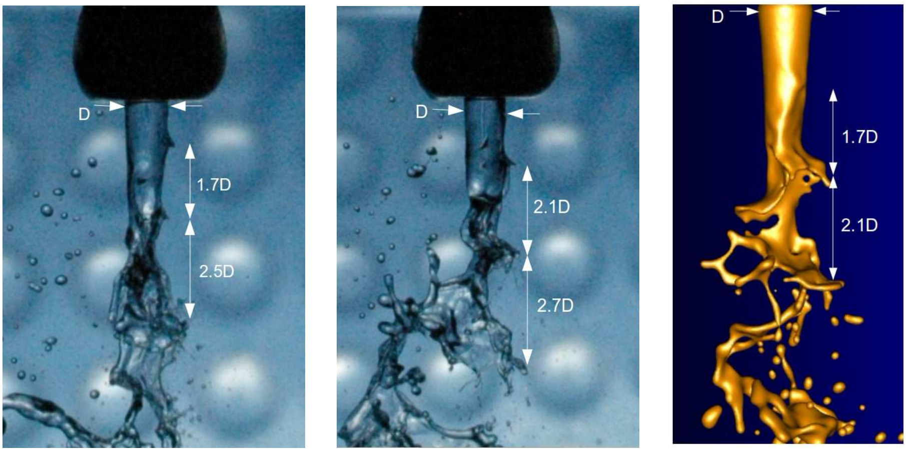

(a) Experiment: Time 1 (b) Experiment: Time 2 (c) Simulation

FIG. 16: Measurement of shear instability using photos at two different times during the experiment (a), (b) and a rendering of simulation data (c).

to measure droplet size and velocity. Simulations used a band-growth algorithm (Hermann, 2010) to identify droplets and compute their size and velocity. Using the two methods, probability density functions of drop size were calculated. The results shown in Fig. 17(a) illustrate the excellent agreement in the size of droplets found in our simulations and experiments. The smallest droplets obtained in the simulation have a diameter of approximately 70 μm. This corresponds to about two cells across the droplet, which is the resolution limit for our conservative level set scheme. The agreement between the

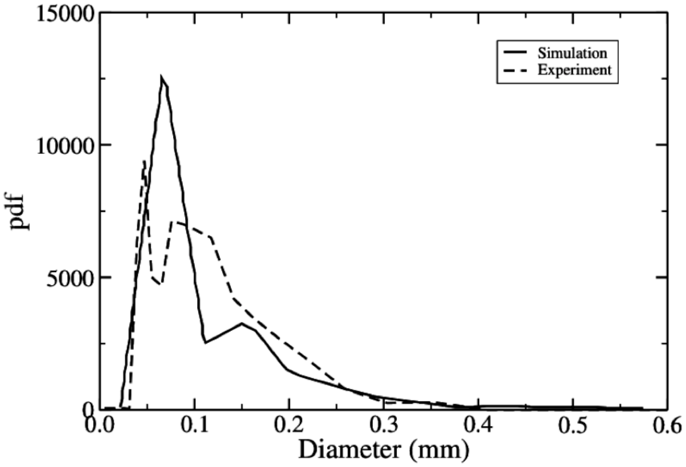

(a) Drop sizes

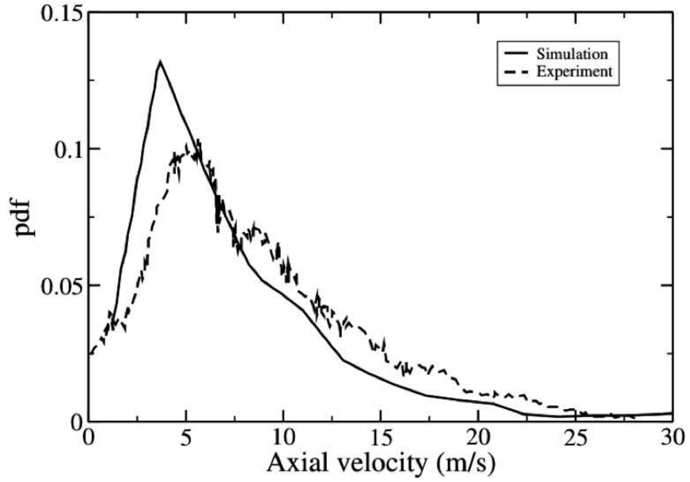

(b) Drop axial velocities

FIG. 17: Probability density function of (a) drop size and (b) drop velocity using experimental and simulation results.

probability density functions suggest that the simulation is capable of accurately capturing the liquid breakup dynamics and could be used to predict drop sizes for design applications.

In addition to drop size distributions, droplet velocity distributions were also calculated. Figure 17(b) shows probability density functions of droplet axial velocity. Again, excellent agreement is found between the experiment and simulation, indicating that the droplets are forming with the correct velocity, which suggests in turn that the breakup mechanism is captured in the simulation.

7. PRIMARY ATOMIZATION OF DIESEL INJECTION

Pressurized fuel injectors are ubiquitous in combustion devices. They achieve efficient atomization by injecting liquid fuel at high velocity in the near-quiescent combustion chamber. The simulation of the breakup of a turbulent liquid jet in quiescent gas is considered in this section.

7.1 Simulation Conditions

The flow configuration is illustrated in Fig. 18. A turbulent liquid is being issued from a nozzle into a quiescent gas. Under the combined effects of inertial, surface tension,

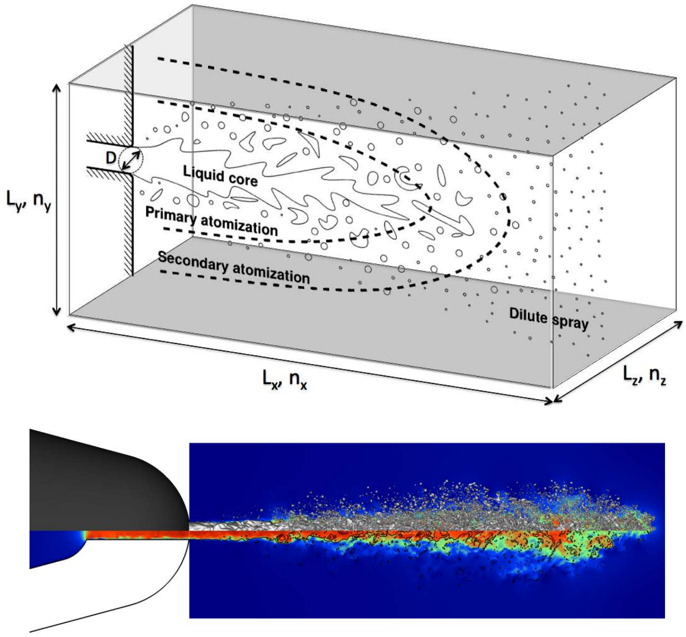

FIG. 18: Flow configuration for the turbulent atomization simulations (top) and typical simulation result (bottom).

and viscous forces, the liquid breaks up into ligaments and droplets. Similar flow configurations have been studied before, see in particular Ménard et al. (2007), Herrmann (2008), Desjardins et al. (2008), and Shinjo and Umemura (2010). The nozzle flow is pre-computed through a preliminary simulation of a realistic single-hole diesel nozzle at a Reynolds number of 5000. This precomputed flow field is then used as inflow conditions for a secondary simulation inside a rectangular domain where the phase interface is tracked.

The reference flow parameters are listed in Table 8. These parameters are characteristic of diesel fuel injection, albeit with increased surface tension and lower Mach number to make the simulations numerically tractable. In addition, Table 8 lists the maximum values for each parameter that were attainable based on the computation resources available. These maximum parameters do not correspond to a single simulation, but rather to a number of distinct simulations, where either a larger domain, a finer mesh, or different flow parameters were considered.

7.2 Simulation Results

Typical simulation results are shown at various times during the liquid injection in Fig. 19, for a $30D \times 10D \times 10D$ domain resolved by a 1536 × 512 × 512 mesh. For both simulations, the Reynolds number based on the inlet jet velocity U_0 and jet diameter D is 5000, while the Weber number varies between 2000 and 5000. This difference in Weber number is equivalent to a factor of 2.5 in surface tension coefficient between

TABLE 8: Range of parameters employed in the diesel injection simulations

Parameters	Reference	Maximum
L_x	$20D$	$45D$
L_y	$5D$	$15D$
L_z	$5D$	$15D$
n_x	1024	2304
n_y	256	768
n_z	256	768
Re = $\rho_l U_0 D/\mu_l$	5000	5,000
We = $\rho_l U_0^2 D/\sigma$	2000	5,000
ρ_l/ρ_g	40	40
μ_l/μ_g	1	2
N_{cell}	67 million	1.61 billion
N_{cell}/D	51.2	100
N_{core}	512	12,288

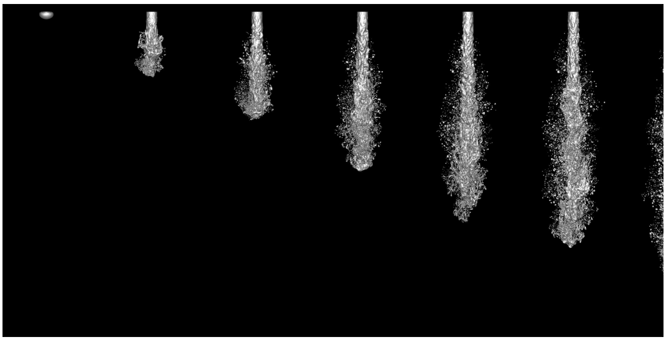

(a) Re = 5000, We = 2000

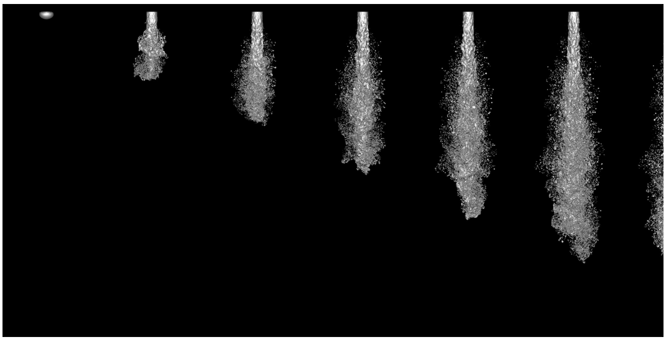

(b) Re = 5000, We = 5000

FIG. 19: Temporal evolution of interface location, turbulent atomization simulations on 402 million cells.

the two simulations (the simulation in the top image in Fig. 19 having a 2.5 times larger surface tension coefficient than the simulation in the bottom image in Fig. 19). In both cases, the liquid jet undergoes rapid breakup, forming numerous ligaments and droplets. However, it can be clearly observed from the high Weber number simulation that reducing the surface tension coefficient leads to a significantly finer spray. Note that this effect is likely to be critical when considering the transition from diesel fuel to biofuels. Indeed, some of the biomass-derived oils considered for fossil fuel displacement have been shown to have a surface tension coefficient two to three times larger than that of standard diesel fuel, and are therefore likely to generate significantly larger droplets when atomized. Of course, this would have direct consequences on the evaporation rate of the fuel, and ultimately in the quality of the subsequent combustion process.

7.3 Scalability Results

The diesel injection simulations presented above are used to analyze the computing performance of NGA, all of which were conducted on Red Mesa, which is a National

Renewable Energy Laboratory (NREL) high-performance computing system located at Sandia National Laboratories in Albuquerque, NM, and devoted exclusively to research and development for renewable energy applications. The system consists of 1920 2.93 GHz dual-socket quad core, Nehalem x5570 processor nodes, for a total of 15,360 cores with a peak performance of 180 TFlops. The nodes are connected via a QDR InfiniBand network arranged as a 3D toroidal mesh. The total aggregate system memory is 23 TB, with more than 1 PB of filesystem space. In addition, note that the Red Mesa infrastructure makes up over a third of the Red Sky/Red Mesa supercomputing system, which was ranked 10th in the Top500 November 2009 Report (www.top500.org).

For all the simulations presented below, NGA is compiled using the Intel Fortran compiler v. 11.1, and OpenMPI v. 1.4.1 is used for the MPI-2.0 libraries. With over 20 different atomization runs conducted on Red Mesa, enough data were generated to explore the scaling properties of NGA in great detail. First, the relative cost of the primary components of NGA is explored. Figure 20 shows the percentage of time spent per time step in the multiphase solver, the velocity solver, and the pressure solver, for a 402 million cell simulation on 4096 cores once it has reached a statistically stationary state. It can be seen that together, these three components of the NGA code account for over 97% of the cost of one time step. The velocity solver naturally presents excellent parallel performance, thanks to the careful use of Message Passing Interface (MPI) communication, and because exact parallel polydiagonal solvers are used for the implicit formulation (Desjardins et al., 2008). If the number of cells per core is taken to be large enough, then local computations should cost significantly more than inter-processor data exchange, which should guarantee excellent scaling. Then, the pressure solver corresponds to the solution of the pressure Poisson equation, which effectively projects the predicted velocity field onto the subspace of velocity fields that are compatible with the continuity equation. Being elliptic in nature, the parallel performance of the Poisson solver is expected to be a limiting factor when assessing both weak and strong scaling properties. Finally, the multiphase solver warrants more considerations. It refers to all the level set manipulations required for successfully tracking

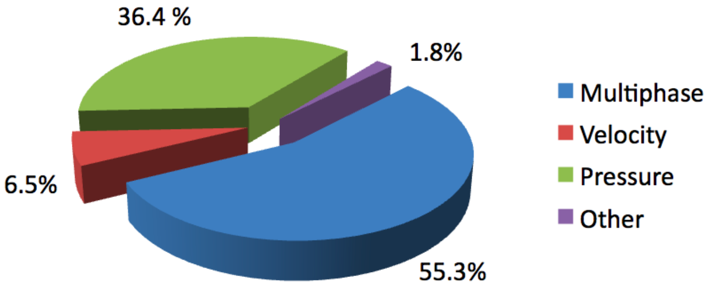

FIG. 20: Proportion of total time taken by time step for a case of fuel atomization on 402 million cells and 4096 cores.

the phase interface, such as level set transport and curvature computation. Two points suggest that the multiphase solver might present somewhat limited scaling. First, the amount of computation depends on the interfacial area located within each core. Since the jets in Fig. 19 expand into a dispersed spray as they move downstream, liquid surface area is likely to vary from core to core, leading to load-balancing issues. Second, a fifth-order accurate scheme is used for the level set transport, which requires a significant increase in the volume of data to be exchanged between cores compared to a second-order scheme, as is being used here for the velocity solver. Here, the multiphase solver represents over 55% of the cost of one NGA time step, which seems compatible with the fact that fuel droplets occupy a large fraction of the computational domain.

Then, scaling properties are considered. Instead of considering strong scaling, or how the code speeds up when increasing the number of cores while keeping the problem size constant (speed-up), we will focus on weak scaling properties by keeping the problem size on each core constant (scale-up). Indeed, the presence of a purely elliptic Poisson equation in NGA means that each cell is fully coupled to any other cells in the computational domain, no matter the distance separating them. This property tends to hinder the speed-up performance significantly, and as a result NGA is not expected to speed-up well. Hence, the focus will be on scale-up properties. Figure 21 shows the scale-up of each of the runs which have been performed on Red Mesa as a function of the number of cores used. Here, the scale-up is computed as

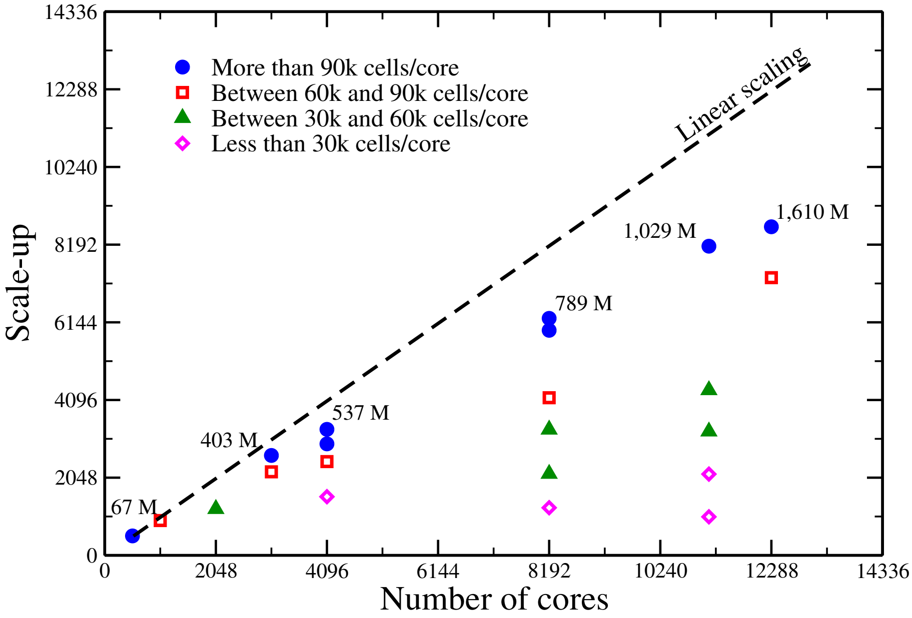

FIG. 21: Scale-up for all the fuel injection NGA runs on Red Mesa.

$$\text{Scale-up} = N_{\text{core}}^{\text{ref}} \left(\frac{n_x n_y n_z}{t_{\text{step}}} \right) \left(\frac{n_x^{\text{ref}} n_y^{\text{ref}} n_z^{\text{ref}}}{t_{\text{step}}^{\text{ref}}} \right)^{-1} , \tag{41}$$

where t_{step} is the time per time step, and the "ref" quantities correspond to the reference simulation, a 67 million cell run on 512 cores, for which the parameters are given in Table 8.

While the dashed line shows linear scaling, the various runs are identified by a symbol and color depending on the number of cells per core. Four categories have been chosen, namely less than 30,000 cells per core (purple diamonds), between 30,000 and 60,000 cells per core (green triangles), between 60,000 and 90,000 cells per core (red squares), and finally more than 90,000 cells per core (blue circles). It appears clearly that the smaller the number of cells per core, the larger the departure from the linear solution. Considering only the runs on more than 90,000 cells per core, one can see that NGA retains excellent scaling properties, even on such a scale. The largest run, a 1.61 billion cell run conducted on 12,288 cores (80% of Red Mesa), shows a scale-up value of 8662, corresponding to an efficiency of over 70%. However, when runs are conducted with less cells per core, the scaling properties of NGA are negatively affected. This is due to the increase in the cost of communications compared to the cost of local computations when the local problem size becomes too small, as mentioned at the beginning of the section. Thus, these results are expected, and we can conclude from these tests that provided one has on the order of 10^5 cells per core, NGA will perform very efficiently at least up to 10^9 cells on 10^4 cores.

In all the runs presented in Fig. 21, we never use more than 130,000 cells per core. This value is fairly low, since typical smaller NGA runs are routinely performed with half a million cells per core. Two reasons motivated this choice: first, Red Mesa only provides 1.5 GB of memory per core, and more importantly, the memory footprint of MPI was found to increase significantly relative to the number of cores (on the order of thousands), thus adversely affecting the ability to increase the number of cells per core beyond a certain limit. Through trial and error, 130,000 cells per core was found to be a safe problem size which allowed a run on any number of cores. Considering the results shown in Fig. 21, it seems likely that running with even more cells per core would allow to achieve even better scaling efficiency.

The detailed scaling properties of each of the three main NGA solvers are then presented in Fig. 22. For this graph, only the most efficient runs of Fig. 21 were retained, meaning that all have about 10^5 cells per core. First, it can be observed that the velocity solver exhibits excellent scaling, as was expected. However, since it represents only about 6.5% of the cost of NGA, it does not impact the scaling of the full code notably. The pressure and multiphase solvers have very similar scaling properties, and since these two solvers account for over 90% of the cost of one time step, they control the overall scaling performance of NGA. While they depart from linear scaling as the

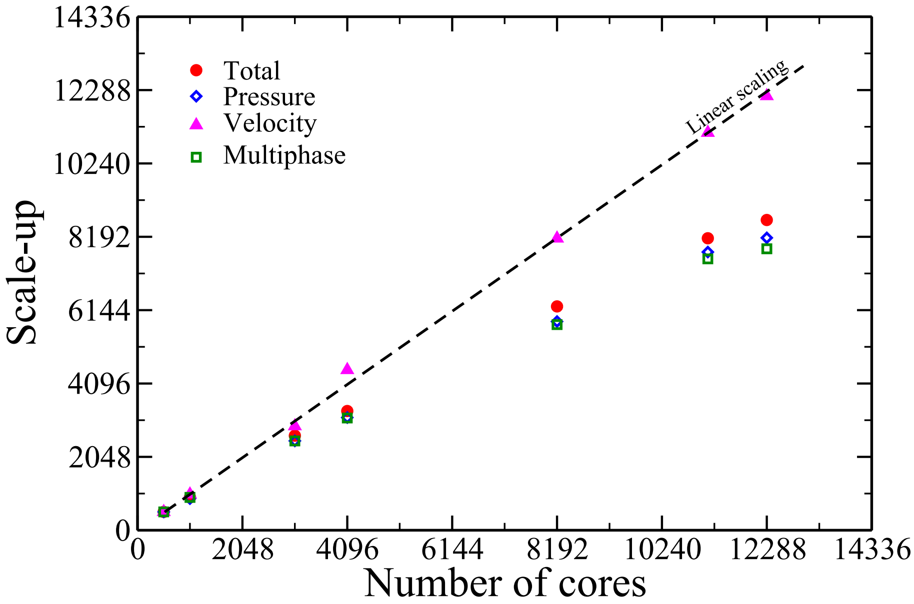

FIG. 22: Scale-up of each of the three main solvers for various NGA runs with about 10^5 cells per core on Red Mesa.

problem size increases, this departure remains limited even on over 10^4 cores. As suggested by Fig. 21, it is likely that the scaling performance would improve by running with larger problem sizes on each core.

Finally, the dependence of the scaling efficiency on the number of cells per core is shown explicitly by presenting a reduced time per time step of NGA as a function of the number of cells per core in Fig. 23. This reduced time is computed as

$$\text{Reduced time} = \frac{t_{\text{step}} N_{\text{core}}}{n_x n_y n_z}, \tag{42}$$

and should therefore be constant if NGA scales linearly. Figure 23 shows that this reduced time tends to a constant (about 50 μs, dashed line) when the number of cells per core becomes large enough.

8. TOWARD SIMULATIONS OF REALISTIC INJECTOR GEOMETRIES

The simulations presented so far have considered atomization problems with fairly simply injector geometries. We now turn our attention to atomizing flows in complex geometries. For the cases presented below, experimental data are not available, hence the focus is on showcasing the simulation capability of the proposed strategy as well as qualitative discussion of the simulation results.

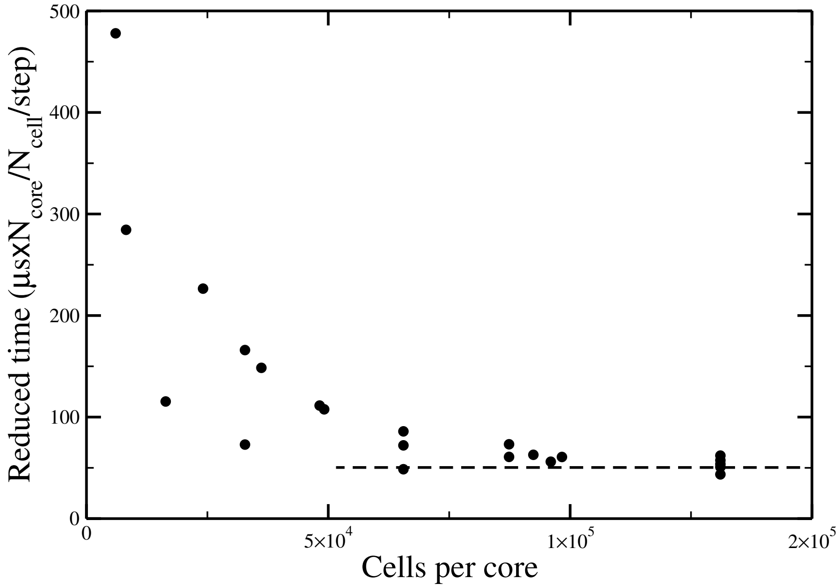

FIG. 23: Reduced time per time step for the atomization simulations as a function of the number of cells per core. Dashed line is 50 μs.

8.1 Pressure Swirl Injection

A pressure swirl fuel injector is simulated, in order to ensure that NGA is capable of predicting the formation of the spray hollow cone and air core inside the pressure swirler. The geometry considered for this case is shown in Fig. 24, and consists of a pipe connected to four swirl vanes feeding into a converging-diverging nozzle. The simulation parameters are summarized in Table 9. The simulation is performed during 48 h on 480

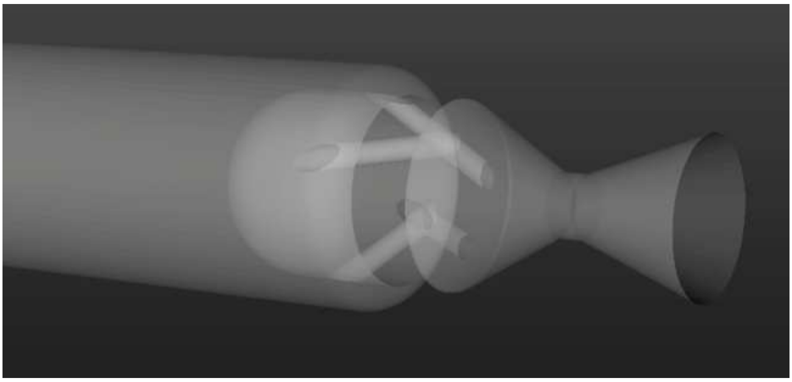

FIG. 24: 3D view of the computed pressure swirl injector geometry.

TABLE 9: Parameters for the pressure swirl simulation

Computational mesh	
Cells in x-direction, nx	512
Cells in y-direction, ny	256
Cells in z-direction, nz	256
Fluids	
Liquid	Water
Gas	Air
Various operating conditions	
Liquid flow rate	0.04 kg/s
Nozzle exit diameter	1.75 cm

compute cores, leading to 13,000 time steps, which corresponds to approximately 100 ms of data at a CFL of 0.9.

The resulting instantaneous flow is shown in three dimensions in Fig. 25, and in Fig. 26 on a 2D cut plane.

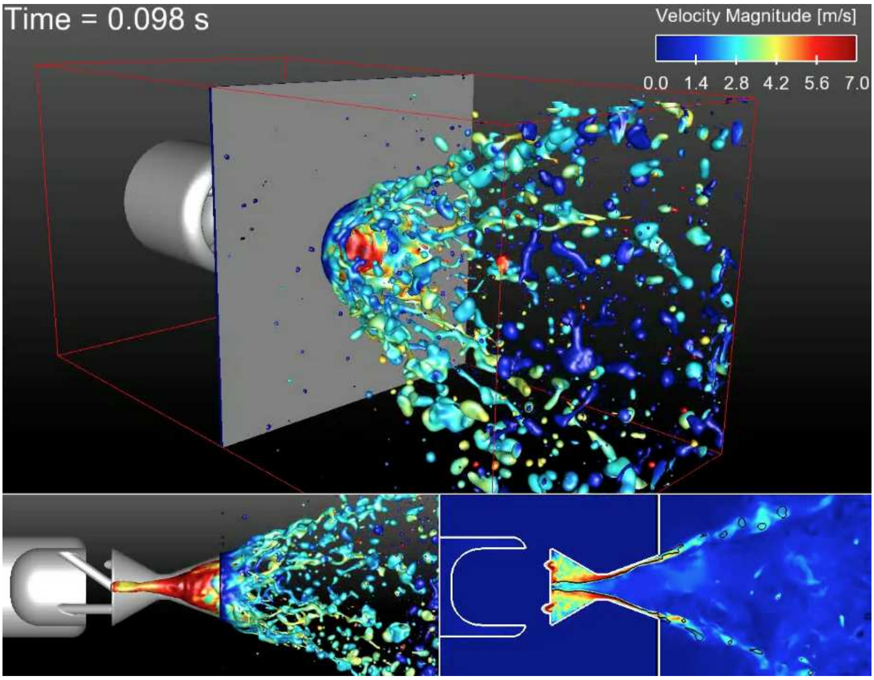

FIG. 25: 3D view of the computed interface location and velocity for the pressure swirl injection simulation.

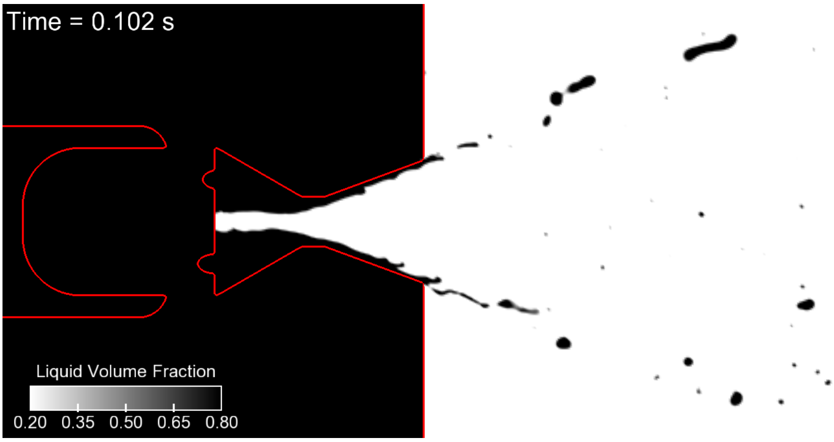

(a) Instantaneous liquid volume fraction field

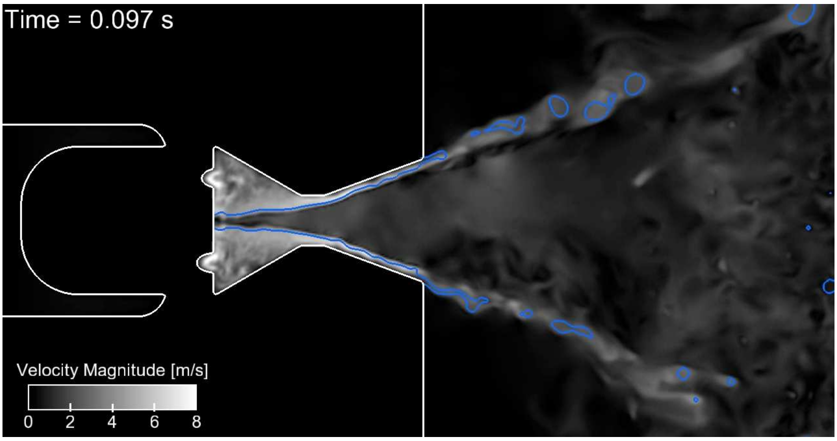

(b) Instantaneous velocity magnitude and interface location

FIG. 26: 2D snapshot of the liquid-gas flow in the pressure swirl injection simulation.

These flow visualizations clearly illustrate that a conical liquid sheet forms at the exit of the pressure swirl, as expected. Due to the turbulence in the flow, the liquid sheet breaks up into ligaments that further break up into droplets very rapidly. The nozzle cavity of the pressure swirl injector fills up with an air core that extends to the back wall of the injector nozzle. This air cavity is robust, although it can be seen to describe a precessing motion. In addition, liquid waves form at the surface of the liquid film that covers the wall of the injector. These results are in good agreement with expectations, although a detailed comparison with experiments remains to be accomplished. Even for such a complex flow simulation, the cost of meshing has been eliminated, and only 20,000 core-hours have been expended using the proposed strategy.

8.2 Dual Orifice Air-Blast Injection

The last case considered exhibits a very complex geometry, including a primary liquid flow through a pressure swirl atomizer (labeled pl for primary liquid), a secondary coaxial, annular, swirled, liquid flow (labeled sl for secondary liquid), and a tertiary coaxial, annular, swirled, gas flow (labeled tg for tertiary gas). The pressure swirl atomizer corresponds to the geometry studied above. The computational geometry considered starts upstream of the swirl vanes, and extends down to the beginning of the combustor dump region. A full 3D view of the injector as an isosurface of the level set function G is shown in Fig. 27. A 2D cut of the geometry is also visible in Fig. 28.

The fluids are taken to be water for the liquid, and ambient air for the gas. The various flow parameters are detailed in Table 10. The time-step size is taken to be $\Delta t = 2$ μs. Simulations are conducted on 576 compute cores for approximately 50 ms.

While NGA can simulate a flow in this complex geometry using the conservative IB scheme described above, a preprocessing step that calculates G from a CAD file representing the injector is necessary. This is accomplished by projecting every cell centroid onto a collection of triangles representing the geometry (as provided in the stereolithography (STL) format automatically). As this step is embarrassingly parallel, it only takes a few minutes on a few hundred cores even for meshes consisting of billions of cells.

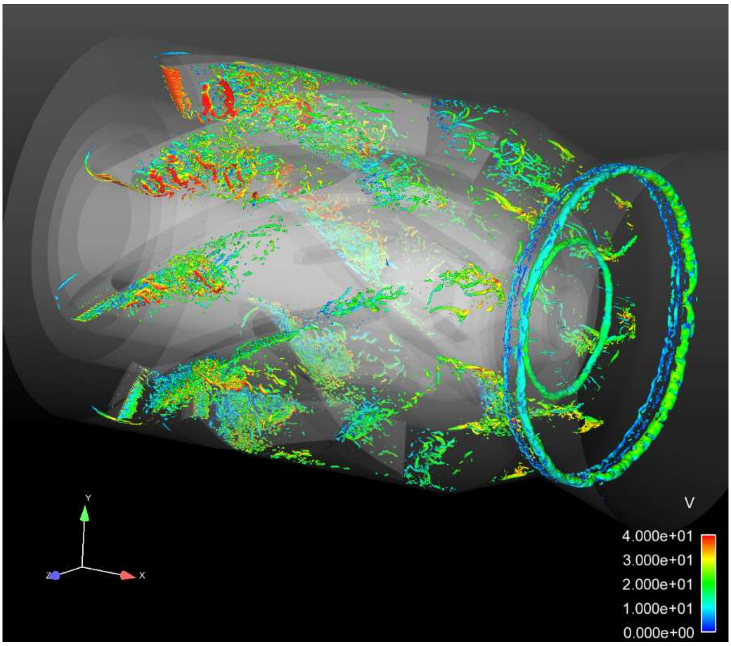

FIG. 27: 3D view of the computed dual-orifice geometry. Instantaneous vortical structures are shown using a positive isosurface of the Q criterion at an early time.

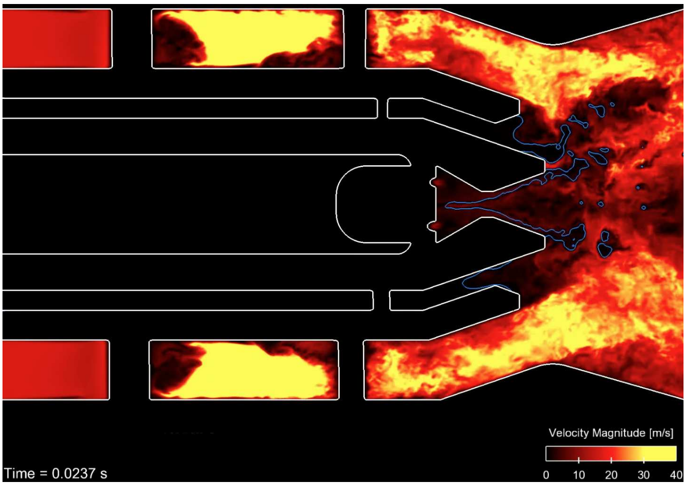

FIG. 28: 2D view of the computed interface location and geometry for the dual orifice injector simulation. The cut plane is colored by the velocity magnitude.

TABLE 10: Flow parameters for the dual orifice injector simulation

Computational Mesh	
Cells in x-direction, nx	1536
Cells in y-direction, ny	1024
Cells in z-direction, nz	1024
Fluids	
Liquid	Water
Liquid density, ρ_l	1000 kg/m^3
Liquid dynamic viscosity, μ_l	1.137×10^{-3} kg/(m · s)
Gas	Air
Gas density, ρ_g	1.226 kg/m^3
Gas dynamic viscosity, μ_g	1.780×10^{-5} kg/(m · s)
Surface tension coefficient, σ	0.0728 N/m
Operating Conditions	
Primary liquid flow rate, $\dot{m}_{pl}$	0.04 kg/s
Primary liquid bulk velocity, U_{pl}	0.166 m/s
Secondary liquid flow rate, $\dot{m}_{sl}$	0.03 kg/s
Secondary liquid bulk velocity, U_{sl}	0.0808 m/s
Tertiary gas flow rate, $\dot{m}_{tg}$	0.04 kg/s
Tertiary gas bulk velocity, U_{tg}	17.09 m/s

Toward the end of the simulation, the flow field is fully turbulent and has reached statistical stationarity. The resulting two-phase flow field is shown on a 2D cut plane in Fig. 28 and in three dimensions in Fig. 29. As for the isolated pressurized injector, a hollow cone forms, as expected. An air core forms that extends to the back wall of the pressure swirler. The swirling turbulent flow field from the outer passage interacts in a complex manner with the spray cone. The secondary passage does not seem to form a hollow cone, and seems to dribble downstream instead. This behavior might be due to an excessively low mass flow rate in the second passage.

9. CONCLUSION

A computational strategy that tackles some of the many challenges of simulating liquid atomization from realistic injectors is presented. The main obstacles identified are (i) multiscale turbulent processes that require a high level of resolution for both the velocity field and the phase interface, (ii) discontinuous fluid properties and a singular surface tension force at the interface, (iii) high-density ratios found in liquid fuel applications that lead to inconsistencies between mass and momentum transport, and (iv) complex geometries of injection systems that are difficult to accommodate in a scalable computing environment. A numerical framework is laid out that systematically addresses each

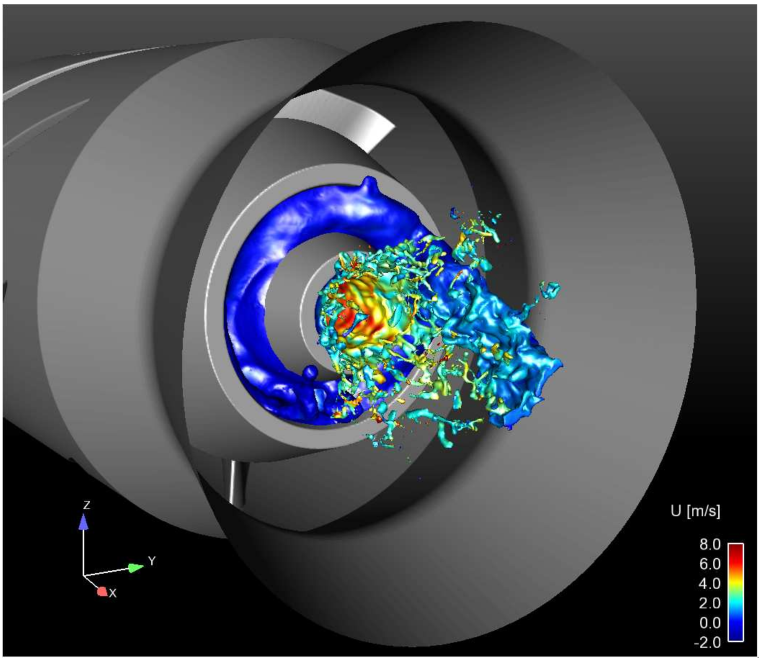

FIG. 29: Three-dimensional view of the computed interface location for the dual orifice injector simulation. The phase interface is colored by the axial velocity.

of the aforementioned issues, offering possible solutions that can allow for robust simulation of multiphase flows that provide insight into the complex physics of turbulent atomization. The turbulent flow field is simulated in the context of DNS and LES using a high-order, fully conservative finite difference code (Desjardins et al., 2008) shown to have excellent parallel performance. Interfacial discontinuities are dealt with through the GFM (Fedkiw et al., 1999), and the interface is transported using a conservative level set method (Desjardins et al., 2008). A density-based momentum flux correction scheme is implemented that leads to improved robustness and accuracy for simulations with high-density ratios and high shear. A conservative IB method is presented that allows for complex geometries to be accounted for on structured grids, so that mesh generation remains trivial. A series of simulations is presented, first confirming the ability of the proposed approach to capture instabilities that are crucial to the atomization process. Then, simulations of both planar and coaxial air-assisted injectors are presented, demonstrating good agreement with theoretical and experimental results. Following experimental validation, simulations of increasing complexity are presented, providing qualitative insight on pressurized, pressure swirl, and air-blast injection processes.

ACKNOWLEDGMENTS

Funding by NAVAIR Propulsion & Power SBIR Phase I contract no. N68335-10-C-0263 and General Electric Global Research is gratefully acknowledged. Computational resources from XSEDE and the National Renewable Energy Laboratory Computational Sciences Center, which is supported by the Office of Energy Efficiency and Renewable Energy of the US Department of Energy under contract no. DE-AC36-08GO28308, are gratefully acknowledged.

REFERENCES

Adalsteinsson, D. and Sethian, J. A., The fast construction of extension velocities in level set methods, *J. Comput. Phys.*, vol. **148**, no. 1, pp. 2–22, 1999.

Agbaglah, G., Delaux, S., Fuster, D., Hoepffner, J., Josserand, Ch., Popinet, S., Ray, P., Scardovelli, R., and Zaleski, S., Parallel simulation of multiphase flows using octree adaptivity and the volume-of-fluid method, *C. R. Méc.*, vol. **339**, nos. 2-3, pp. 194–207, 2011.

Apte, S. V., Mahesh, K., and Gorokhovski, M., Stochastic modeling of atomizing spray in a complex swirl injector using large eddy simulation, *Proc. Combust. Inst.*, vol. **32**, no. 2, pp. 2257–2266, 2009.

Apte, S. V., Mahesh, K., and Moin, P., Large-eddy simulation of evaporating spray in a coaxial combustor, *Proc. Combust. Inst.*, vol. **32**, no. 2, pp. 2247–2256, 2009.

Aslam, T. D., A level-set algorithm for tracking discontinuities in hyperbolic conservation laws: I. Scalar equations, *J. Comput. Phys.*, vol. **167**, no. 2, pp. 413–438, 2001.

Boeck, T., Li, J., López-Pagés, E., Yecko, P., and Zaleski, S., Ligament formation in sheared liquidgas layers, *Theor. Comput. Fluid Dyn.*, vol. **21**, no. 1, pp. 59–76, 2006.

Brackbill, J. U., Kothe, D. B., and Zemach, C., A Continuum Method for Modeling Surface Tension, *J. Comput. Phys.*, vol. **100**, no. 2, pp. 335–354, 1992.

Brady, P. T., Herrmann, M., and Lopez, J. M., Code verification for finite volume multiphase scalar equations using the method of manufactured solutions, *J. Comput. Phys.*, vol. **231**, no. 7, pp. 2924–2944, 2012.

Chen, S., Merriman, B., Osher, S., and Smereka, P., A simple level set method for solving stefan problems, *J. Comput. Phys.*, vol. **135**, no. 1, pp. 8–29, 1997.

Dendy, J. E., Black box multigrid, *J. Comput. Phys.*, vol. **48**, no. 3, 366–386, 1982.

Dendy, J. E., Black box multigrid for nonsymmetric problems, *Appl. Math. Comput.*, vol. **13**, nos. 3-4, pp. 261–283, 1983.

Dendy, J. E., Black box multigrid for systems, *Appl. Math. Comput.*, vol. **19**, nos. 1-4, pp. 57–74, 1986.

Dendy, J. E., Black box multigrid for periodic and singular problems, *Appl. Math. Comput.*, vol. **25**, no. 1, pp. 1–10, 1988.

Desjardins, O., Blanquart, G., Balarac, G., and Pitsch, H., High order conservative finite difference scheme for variable density low Mach number turbulent flows, *J. Comput. Phys.*, vol. **227**, no. 15, pp. 7125–7159, 2008.

Desjardins, O. and Moureau, V., Methods for multiphase flows with high density ratio, *in Proc. of the Center for Turbulence Research Summer Program*, pp. 313–322, Stanford, CA, July, 2010.

Desjardins, O., Moureau, V., and Pitsch, H., An accurate conservative level set/ghost fluid method for simulating turbulent atomization, *J. Comput. Phys.*, vol. **227**, no. 18, pp. 8395–8416, 2008.

Desjardins, O. and Pitsch, H., A spectrally refined interface approach for simulating multiphase flows, *J. Comput. Phys.*, vol. **228**, no. 5, pp. 1658–1677, 2009.

Fedkiw, R. P., Aslam, T. D., Merriman, B., and Osher, S., A non-oscillatory Eulerian approach to interfaces in multimaterial flows (the Ghost Fluid Method), *J. Comput. Phys.*, vol. **152**, no. 2, pp. 457–492, 1999.

Fedkiw, R. P., Aslam, T. D., and Xu, S., The ghost fluid method for deflagration and detonation discontinuities, *J. Comput. Phys.*, vol. **154**, no. 2, 393–427, 1999.

Fuster, D., Agbaglah, G., Josserand, Ch., Popinet, S., and Zaleski, S., Numerical simulation of droplets, bubbles and waves: State of the art, *Fluid Dyn. Res.*, vol. **41**, no. 6, pp. 1–24, 2009.

Fuster, D., Bagué, A., Boeck, T., Le Moyne, L., Leboissetier, A., Popinet, S., Ray, P., Scardovelli, R., and Zaleski, S., Simulation of primary atomization with an octree adaptive mesh refinement and VOF method, *Int. J. Multiphase Flow*, vol. **35**, no. 6, pp. 550–565, 2009.

Gorokhovski, M. and Herrmann, M., Modeling primary atomization, *Ann. Rev. Fluid Mech.*, vol. **40**, pp. 343–366, 2008.

Hartmann, D., Meinke, M., and Schröder, W., A strictly conservative Cartesian cut-cell method for compressible viscous flows on adaptive grids, *Comput. Methods Appl. Mech. Eng.*, vol. **200**, nos. 9-12, pp. 1038–1052, 2011.

Herrmann, M., A domain decomposition parallelization of the fast marching method, *Center for Turbulence Research 23 Annual Research Briefs*, pp. 213–225, 2003.

Herrmann, M., Detailed numerical simulations of the primary breakup of turbulent liquid jets, *in Proc. of the 21st Annual Conf. ILASS Americas*, Orlando, FL, May, 2008.

Herrmann, M., A parallel Eulerian interface tracking/Lagrangian point particle multi-scale coupling procedure, *J. Comput. Phys.*, vol. **229**, no. 3, pp. 745–759, 2010.

Hirt, C. W. and Nichols, B. D., Volume of fluid (VOF) method for the dynamics of free boundaries, *J. Comput. Phys.*, vol. **39**, no. 1, pp. 201–225, 1981.

Jones, W. P. and Lettieri, C., Large eddy simulation of spray atomization with stochastic modeling of breakup, *Phys. Fluids*, vol. **22**, no. 11, p. 115106, 2010.

Kang, M., Fedkiw, R. P., and Liu, X.-D., A boundary condition capturing method for multiphase incompressible flow, *J. Sci. Comput.*, vol. **15**, no. 3, pp. 323–360, 2000.

Kerschen, G., Golinval, J.-C., Vakakis, A. F., and Bergman, L. A., The method of proper orthogonal decomposition for dynamical characterization and order reduction of mechanical systems: An overview, *Nonlinear Dyn.*, vol. **41**, nos. 1-3, pp. 147–169, 2005.

Kirkpatrick, M. P., Armfield, S. W., and Kent, J. H., A representation of curved boundaries for the solution of the Navier-Stokes equations on a staggered three-dimensional Cartesian grid, *J. Comput. Phys.*, vol. **184**, no. 1, pp. 1–36, 2003.

Lebas, R., Menard, T., Beau, P. A., Berlemont, A., and Demoulin, F. X., Numerical simulation of primary break-up and atomization: DNS and modelling study, *Int. J. Multiphase Flow*, vol. **35**, no. 3, pp. 247–260, 2009.

Lefebvre, A. H., *Atomization and Sprays*, CRC Press, Boca Raton, FL, 1989.

Losasso, F., Fedkiw, R. P., and Osher, S., Spatially adaptive techniques for level set methods and incompressible flow, *Comput. Fluids*, vol. **35**, no. 10, pp. 995–1010, 2006.

MacCormack, R. W., Iterative modified approximate factorization, *Comput. Fluids*, vol. **30**, nos. 7-8, pp. 917–925, 2001.

MacLachlan, S. P., Tang, J. M., and Vuik, C., Fast and robust solvers for pressure-correction in bubbly flow problems, *J. Comput. Phys.*, vol. **227**, no. 23, pp. 9742–9761, 2008.

Marmottant, P. and Villermaux, E., On spray formation, *J. Fluid Mech.*, vol. **498**, pp. 73–111, 2004.

McCaslin, J. O. and Desjardins, O., A localized re-initialization equation for the conservative level set method, *J. Comput. Phys.*, 2013, in press.

Ménard, T., Beau, P.-A., Tanguy, S., Demoulin, F.-X., and Berlemont, A., Primary break-up: DNS of liquid jet to improve atomization modelling, *Comput. Meth. Multiphase Flow III*, pp. 343–352, 2005.

Ménard, T., Tanguy, S., and Berlemont, A., Coupling level set/VOF/ghost fluid methods: Validation and application to 3D simulation of the primary break-up of a liquid jet, *Int. J. Multiphase Flow*, vol. **33**, no. 5, pp. 510–524, 2007.

Meneveau, Ch., Lund, T. S., and Cabot, W. H., A Lagrangian dynamic subgrid-scale model of turbulence, *J. Fluid Mech.*, vol. **319**, pp. 353–385, 1996.

Meyer, M., Devesa, A., Hickel, S., Hu, X. Y., and Adams, N. A., A conservative immersed interface method for Large-Eddy Simulation of incompressible flows, *J. Comput. Phys.*, vol. **229**, no. 18, pp. 6300–6317, 2010.

Mittal, R. and Iaccarino, G., Immersed boundary methods, *Ann. Rev. Fluid Mech.*, vol. **37**, no. 1, pp. 239–261, 2005.

Moin, P., Large eddy simulation of multi-phase turbulent flows in realistic combustors, *Prog. Comput. Fluid Dyn., Int. J.*, vol. **4**, no. 3, pp. 237–240, 2004.

Noh, W. and Woodward, P., SLIC (simple line interface calculation), *in Proc. of the Fifth Int. Conf. on Numerical Methods in Fluid Dynamics*, pp. 330–340, Enschede, June 28–July 2, 1976.

Oefelein, J. C., 2006 Large eddy simulation of turbulent combustion processes in propulsion and power systems, *Prog. Aerosp. Sci.*, vol. **42**, no. 1, pp. 2–37, 2006.

Olsson, E. and Kreiss, G., A conservative level set method for two phase flow, *J. Comput. Phys.*, vol. **210**, no. 1, pp. 225–246, 2005.

Olsson, E., Kreiss, G., and Zahedi, S., A conservative level set method for two phase flow II, *J. Comput. Phys.*, vol. **225**, no. 1, pp. 785–807, 2007.

Osher, S. and Sethian, J. A., Fronts propagating with curvature-dependent speed: Algorithms based on Hamilton-Jacobi formulations, *J. Comput. Phys.*, vol. **79**, no. 1, pp. 12–49, 1988.

Owkes, M. and Desjardins, O., A discontinuous Galerkin conservative level set scheme for interface capturing in multiphase flows, *J. Comput. Phys.*, vol. **249**, no. 1, pp. 275–302, 2013.

Parker, B. J. and Youngs, D. L., Two and three dimensional Eulerian simulation of uid flow with material interfaces, *UK Atomic Weapons Establishment*, 1992.

Peng, D., Merriman, B., Osher, S., Zhao, H., and Kang, M., A PDE-based fast local level set method, *J. Comput. Phys.*, vol. **155**, no. 2, pp. 410–438, 1999.

Pitsch, H., Desjardins, O., Balarac, G., and Ihme, M., Large-eddy simulation of turbulent reacting flows, *Prog. Aerosp. Sci.*, vol. **44**, no. 6, pp. 466–478, 2008.

Raessi, M., A level set based method for calculating flux densities in two-phase flows, *Center for Turbulence Research Annual Research Briefs*, pp. 467–478, 2008.

Raessi, M. and Pitsch, H., Modeling interfacial flows characterized by large density ratios with the level set method, *Center for Turbulence Research Annual Research Briefs*, pp. 159–169, 2009.

Rayana, F. B., *Contribution à létude des instabilités interfaciales liquide-gaz en atomisation assistée et tailles de gouttes*, PhD Thesis, Institute National Polytechnique de Grenoble, Grenoble, France, September 8–11, 2007.

Rayana, F. B., Cartellier, A., and Hopfinger, E. Assisted atomization of a liquid layer: Investigation of the parameters affecting the mean drop size prediction, *in Proc. Int. Conf. Liquid Atomization and Spray Systems (ICLASS)*, pp. 1–8, Kyoto, Japan, August 27–Sept. 1, 2006.

Raynal, L., Villermaux, E., Lasheras, J. C., and Hopfinger, E. J., Primary instability in liquid-gas shear layers, *11th Symp. on Turbulent Shear Flows*, vol. **3**, pp. 27.1–27.5, 1997.

Rudman, M., Volume-tracking methods for interfacial flow calculations, *Int. J. Numer. Methods Fluids*, vol. **24**, no. 7, pp. 671–691, 1997.

Rudman, M., A volume-tracking method for incompressible multifluid flows with large density variations, *Int. J. Numer. Methods Fluids*, vol. **28**, pp. 357–378, 1998.

Sander, W. and Weigand, B., Direct numerical simulation and analysis of instability enhancing parameters in liquid sheets at moderate Reynolds numbers, *Physics of Fluids*, vol. **20**, no. 5, p. 053301, 2008.

Scardovelli, Ruben and Zaleski, S., Direct numerical simulation of free-surface and interfacial flow, *Ann. Rev. Fluid Mech.*, vol. **31**, no. 1, pp. 567–603, 1999.

Sethian, J. A., A fast marching level set method for monotonically advancing fronts, *Proc. Nat. Acad. Sci.*, vol. **93**, no. 4, pp. 1591–1595, 1996.

Sethian, J. A., Fast marching methods, *SIAM Rev.*, vol. **41**, pp. 199–235, 1999.

Sethian, J. A., *Level Set Methods and Fast Marching Methods: Evolving Interfaces in Computational Geometry, Fluid Mechanics, Computer Vision, and Materials Science*, Cambridge University Press, Cambridge, 1999.

Shapira, Y., *Matrix-Based Multigrid: Theory and Applications*, Springer, Berlin, 2008.

Shinjo, J. and Umemura, A., Simulation of liquid jet primary breakup: Dynamics of ligament and droplet formation, *Int. J. Multiphase Flow*, vol. **36**, no. 7, pp. 513–532, 2010.

Sussman, M., Smereka, P., and Osher, S., A level set method for computing solutions to incompressible two-phase flow, *J. Comput. Phys.*, vol. **114**, pp. 146–159, 1994.

Van der Vorst, H. A. and Dekker, K., Conjugate gradient type methods and preconditioning, *J. Comput. Appl. Math.*, vol. **24**, nos. 1-2, pp. 73–87, 1988.

Van der Vorst, H. A., The performance of FORTRAN implementations for preconditioned conjugate gradients on vector computers, *Parallel Comput.*, vol. **3**, no. 1, pp. 49–58, 1986.

van Poppel, B. P., Desjardins, O., and Daily, J. W., A ghost fluid, level set methodology for simulating multiphase electrohydrodynamic flows with application to liquid fuel injection, *J. Comput. Phys.*, vol. **229**, no. 20, pp. 7977–7996, 2010.

Villermaux, E., Mixing and spray formation in coaxial jets, *J. Propuls. Power*, vol. **14**, no. 5, pp. 807–817, 1998.

Villiers, E. D., Gosman, A., and Weller, H. G., Large eddy simulation of primary diesel spray atomization, *SAE Trans.*, vol. **113**, no. 3, pp. 193–206, 2004.

Vuorinen, V. A., Hillamo, H., Kaario, O., Nuutinen, M., Larmi, M., and Fuchs, L., Effect of droplet size and atomization on spray formation: A priori study using large-eddy simulation, *Flow, Turbul. Combust.*, vol. **86**, nos. 3-4, pp. 533–561, 2010.

Wang, Y., Liu, X., Im, K.-S., Lee, W.-K., Wang, J., Fezzaa, K., Hung, D. L. S., and Winkelman, J. R., Ultrafast X-ray study of dense-liquid-jet flow dynamics using structure-tracking velocimetry, *Natur. Phys.*, vol. **4**, no. 4, pp. 305–309, 2008.

Weber, C., Disintegration of liquid jets, *Z. Angew. Math. Mech.*, vol. **11**, no. 2, pp. 136–159, 1931.

www.top500.org., access date is November, 2009.